Section B

FLUID MECHANICS

INFLUENCE OF DUCT CROSS-SECTION ON THE FLOW CHARACTERISTICS AROUND A SMOOTH SPHERE

Ž. Stamenković [1], J. Bogdanović-Jovanović[2]

[1] Faculty of Mechanical Engineering,
University of Nis, Aleksandra Medvedeva 14, 18000 Nis
e-mail: zikas@masfak.ni.ac.rs
[2] Faculty of Mechanical Engineering,
University of Nis, Aleksandra Medvedeva 14, 18000 Nis
e-mail: bminja@masfak.ni.ac.rsInstitute of Mechanics

Abstract. In this paper experimental and numerical investigations of the fluid flow around a smooth sphere placed in a quadratic cross section duct are represented. Experimental measurements are carried out using a Laser-Doppler Anemometer (LDA), and numerical simulation results are obtained by solving RANS equations using different turbulence models (k-ε, k-ω, BSL and BSL transition gamma theta model) of the fluid flow around a smooth sphere. In order to provide information on turbulent flow structures and spectral distribution Detached Eddy Simulation Model is used. Experimental and numerical results of flow velocity fields were compared for the case of the turbulent subcritical flow regime around a smooth sphere ($Re<3\cdot10^5$). The objective of this investigation was to determine an influence of duct cross-section range on the flow characteristics around the smooth sphere, particularly on the boundary layer separation point.

1. Introduction

Numbering investigation of flow around bluff bodies (in which the body length in the flow direction is close to or equal to the length perpendicular to the flow direction) have been carried out, due to its huge practical interest. Firstly, it started mostly as experimental investigation, in conjunction with theoretical consideration. Nowadays, with increased application of CFD codes, numerical simulations have become equally important tool for engineering and scientific work and substitute for multiple repeat of experiments.
The location of the onset and extent of transition are of major importance in the design and performance of many devices where the wall-shear-stress or wall heat transfer is of interest. The transition process can also have a strong influence on the separation behavior of boundary layers. As a result, transition can have a large effect on the performance of airfoils and bluff bodies. There are a number of different transition mechanisms depending on the turbulence level of the external flow, the pressure gradient along the laminar boundary layer, the geometrical details, the surface roughness, etc.
In this study has been investigated the class of separated bluff body flow – flow around a smooth sphere, which represents a complex case characterized by large-scale vortex shedding, transitional shear layers, and a turbulent wake with random and periodic Reynolds stresses of comparable magnitudes. Significant research effort has been made into

studying the flow past a stationary sphere over a wide range of Reynolds numbers both experimentally (Achenbach [1], Taneda [2,3], Bakic [4]) and numerically (Constantinescu and Squires [5], Johnson and Patel [6], Mittal [7], Tomboulides and Orszag [8], Ploumhans et. al. [9], Yun et. al. [10] and others).
The main interest was the investigation of the fluid flow around a smooth sphere in subcritical turbulent regime, experimentally and using numerical simulations. Experimental measurements of fluid flow velocity field around the smooth sphere were performed using a Laser-Doppler Anemometry (LDA), in the Fluid Mechanics Laboratory at the Faculty of Mechanical Engineering in Nis. For numerical simulations Ansys CFD code is used, which is considered as one of the most reliable commercial software.
After the validation of numerical model and determination of the most appropriate turbulence model for the case of fluid flow around a smooth sphere, it was also made an effort to numerically investigate different duct cross-section size, in order to examine its influence on the flow around the smooth sphere.

2. Experimental setup

Laser-Doppler Anemometry is a contemporary method of measuring flow velocity, using the Doppler effect of frequency changing of the light scattered from the moving particle in the fluid flow, which does not disturb the flow in the measuring area. Therefore this method is non-intrusive (contactless), based on optical technique. In addition, it is absolute measurement technique and no calibration is required, provided very high accuracy. LDA measurements require traces particles seeded in the fluid flow, and for the water from public water supply (containing enough amount of small particles) this condition is already satisfied.
The special properties of the gas laser, which provides monochromatic, coherent, linearly polarized light wave of low-divergence beam (Gaussian distribution), make the LDA appropriate and highly accurate method for flow velocity measurements [11,12].
Experimental test set used for laboratory measurements is with open water circulation, and it is chematicly shown in Fig.1.

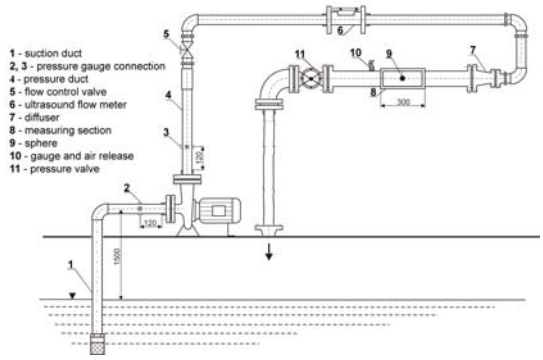

Figure 1. Setup of the LDA test set.

Figure 2. Measuring section of LDA test set.

For the measurements of water velocity around the smooth sphere at the designed test set was used one component backscatter DANTEC laser-Doppler system, (Flowlite LDA),

consists of laser He-Ne probe (power of 10 mW and wave length of λ=632,8 nm), optical cable, laser unit and BSA F60 signal processor in coincidence mode. Basic operating parameters of LDA system are: the measuring volume is 0,05x0,05x0,43mm ($\delta_x=\delta_y$=0,05mm, δ_z=0,43mm), the distance between the laser beams at the transmitting lens is 38,4 mm, Gaussian beam diameter d_o=2,2 mm (beam "waist") and the focal length of the laser beam is 160mm. LDA system is directly connected to the signal processor, which transmits information to the computer, where special software processes compute data in real time. Measured velocity values at any point of flow domain are obtained either by direct software process of the signal or as a product of Doppler frequency (f_d) and calibration constant of LDA system (c).
In addition to the centrifugal pump, which operates at the best efficiency point (pump flow rate Q=90 l/s and pump head H=35m), experimental test set includes pressure gauges and ultrasonic flow meter.
Owing to the existed (and modified) pump examination test set, especially owing to pump characteristics, the LDA measurements were carried out for fluid flow around the sphere of the diameter 40mm, placed in the quadratic duct dimensions 75x75mm.
Reynolds number of the free stream was Re~$3\cdot10^4$, and the Reynolds numbers related to the sphere diameter is ~$1{,}5\cdot10^4$ (local Reynolds number for the sphere is ~$2\cdot10^4$, where the characteristic velocity is mean velocity in the cross section from the sphere to the duct wall).

3. Numerical simulation of the fluid flow around a smooth sphere

Two numerical approaches are used in this study: solving RANS equations (Reynolds-averaged Navier–Stokes equations, averaged in time) and solving Detached Eddy Simulation model (DES model, which are transient simulations dependent on time changes).
Regarding the first approach, four turbulence models are used in RANS simulations: k-ε, k-ω, BSL and BSL transition gamma theta model. First two models are used only in order to compare the velocity profiles with velocities obtained with LDA measurement.
The BSL, BSL transition and DES model are used for determination of boundary layer separation point. The BSL model is designed to give results similar to those of the original k-omega model of Wilcox, but without its strong dependency on arbitrary free stream values. The BSL model is identical to the Wilcox model in the inner 50 percent of the boundary-layer but changes gradually to the high Reynolds number Jones-Launder k-epsilon model (in a k-ω formulation) towards the boundary-layer edge.
Engineering transition predictions are based mainly on two modeling concepts. The first is the use of low-Reynolds number turbulence models, where the wall damping functions of the underlying turbulence model trigger the transition onset. This concept is attractive, as it is based on transport equations and can therefore be implemented without much effort. However, experience has shown that this approach is not capable of reliably capturing the influence of the many different factors that affect transition, such as free-stream turbulence, pressure gradients and separation. The second approach is the use of experimental correlations. The correlations usually relate the turbulence intensity, in the free-stream to the momentum-thickness Reynolds number at transition onset. Langrty and Menter [13] developed a locally formulated transport equation for intermittency, which can be used to trigger transition. The full model is based on two transport equations, one for the

intermittency and one for the transition onset criteria in terms of momentum thickness Reynolds number. It is called the BSL "Gamma Theta Model" and is the recommended transition model for general-purpose applications. It uses a new empirical correlation that has been developed to cover standard bypass transition as well as flows in low free-stream turbulence environments. This built-in correlation has been extensively validated for a wide range of transitional flows.

In an attempt to improve the predictive capabilities of turbulence models in highly separated regions, Spalart [14] proposed a hybrid approach, which combines features of classical RANS formulations with elements of Large Eddy Simulations (LES) methods. The concept has been termed Detached Eddy Simulation (DES) and is based on the idea of covering the boundary layer by a RANS model and switching the model to a LES mode in detached regions. The present version of the DES model is based on the SST formulation. The advantage of this combination is that the accurate prediction of turbulent boundary layers up to separation and in mildly separated regions carries over from the SST model. In addition, the SST model supports the formulation of a zonal DES formulation, which is less sensitive to grid resolution restrictions than the standard DES formulation. Compared to classical LES methods, DES saves orders of magnitude of computing power for high Reynolds number flows. Though this is due to the moderate costs of the RANS model in the boundary layer region, DES still offers some of the advantages of an LES method in separated regions.

3.1. Numerical model

The first step in numerical simulation is creating geometry models for different sizes of the quadratic measuring section, consist of simple geometry shapes (quadratic duct and smooth sphere in the middle). The smooth sphere was placed in the middle of the domain (i.e. measuring section) in all duct models.

Further, the mesh is created, taking into account the structure of the mesh, especially in the area around the sphere. According to the mesh elements number, all meshes differ, however, the mesh created around the sphere is very similar for all different cases. The behavior of the meshes near the sphere is illustrated in Fig. 3. The meshes are made fine nearer the sphere and the walls and made coarse in the free stream. A pentahedron (prism meshes) is created for the surfaces of the walls and the sphere, taking the boundary layer into consideration. The number of mesh elements varies between 500000 and 2800000 elements (tetrahedron and prisms, whereat prismatic mesh elements are generated around all solid boundaries of the fluid flow domain).

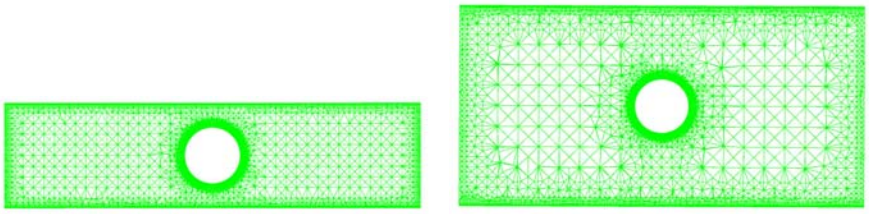

Figure 3. Unstructured discretization mesh for different duct cross-section sizes: 75 mm and 150 mm.

Once the fluid domain has been meshed, the governing equations (in integral form) are applied to each discrete control volume and used to construct a set of non-linear algebraic equations for the discrete dependent variables. Calculation procedure stores discrete values of the variables at the cell centers, however values of the variables are required at the cell faces for the convection terms in the equations and these must be interpolated from the cell centre values. This is accomplished using an high resolution scheme, where the advective flux is evaluated using the values from the upwind node, based on the boundedness principles used by Barth and Jesperson [15]. Numerical simulations convergence criteria were that root mean square values of the equation residuals are lower than 10^{-5}.

3.2 Mathematical formulation of turbulence models

In this study are used four turbulence models for solving RANS simulations: k-ε, k-ω, BSL and SST model.
In the standard k-ε turbulence model, values of turbulence kinetic energy (k), and turbulence eddy dissipation (ε) are obtained by using following differential equations:

$$\frac{\partial(\rho k)}{\partial t}+\nabla(\rho \mathbf{U}k)=\nabla\left[\left(\mu+\frac{\mu_t}{\sigma_k}\right)\nabla k\right]+P_k-\rho\varepsilon\,, \tag{1}$$

$$\frac{\partial(\rho \varepsilon)}{\partial t}+\nabla(\rho \mathbf{U}\varepsilon)=\nabla\left[\left(\mu+\frac{\mu_t}{\sigma_\varepsilon}\right)\nabla \varepsilon\right]+\frac{\varepsilon}{k}\left(C_{\varepsilon 1}P_k-C_{\varepsilon 2}\rho\varepsilon\right), \tag{2}$$

where μ_t is the turbulent viscosity $\mu_t=\rho C_\mu k^2/\varepsilon$, $C_\mu, C_{\varepsilon 1}, C_{\varepsilon 2}, \sigma_k$ and σ_ε are model constants ($C_\mu=0,09$, $C_{\varepsilon 1}=1,44$, $C_{\varepsilon 2}=1,92$, $\sigma_k=1$, $\sigma_\varepsilon=1,3$) and P_k is the turbulence production due to viscous and buoyancy forces, which is modeled using:

$$P_k=\mu_t\nabla\mathbf{U}\left(\nabla\mathbf{U}+\nabla\mathbf{U}^T\right)-\frac{2}{3}\nabla\mathbf{U}\left(3\mu_t\nabla\mathbf{U}+\rho k\right). \tag{3}$$

The k-ω turbulence model's assumptions is that the turbulent viscosity is linked to the turbulence kinetic energy (k) and turbulent frequency (ω) via the relation $\mu_t=\rho k/\omega$,

$$\frac{\partial(\rho k)}{\partial t}+\nabla(\rho \mathbf{U}k)=\nabla\left[\left(\mu+\frac{\mu_t}{\sigma_k}\right)\nabla k\right]+P_k-\beta'\rho k\omega\,, \tag{5}$$

$$\frac{\partial(\rho \omega)}{\partial t}+\nabla(\rho \mathbf{U}\omega)=\nabla\left[\left(\mu+\frac{\mu_t}{\sigma_\omega}\right)\nabla \omega\right]+\alpha\frac{\omega}{k}P_k-\beta\rho\omega^2\,, \tag{6}$$

where constants are: β'=0,09; α=5/9; β=0,075; σ_k=2; σ_ω=2.

The Wilcox k-ω model shows a strong sensitivity for the free-stream condition, and depending on the value specified for ω at the inlet, there can be detected a significant variation in results [16]. On the other hand the k-ε turbulence model shows poor accuracy

for the near-wall region. Therefore, Menter [17] was developed a new turbulence model – BSL turbulence model, blending between the k-ω model near the surface and the k-ε model in the outer region. This requires the transformation of the k-ε model to the k-ω formulation and a subsequent addition of the corresponding equations. The Wilcox model is thereby multiplied by a blending function F_1, and the transformed k-ε model by a function 1-F_1, where F_1 is equal to one near the surface and switches over to zero inside the boundary layer. The corresponding k- and ω - equations are added to give the BSL model:

$$\frac{\partial(\rho k)}{\partial t}+\nabla(\rho \mathbf{U}k)=\nabla\left[\left(\mu+\frac{\mu_t}{\sigma_{k3}}\right)\nabla k\right]+P_k-\beta'\rho k\omega\,, \tag{7}$$

$$\frac{\partial(\rho\omega)}{\partial t}+\nabla(\rho \mathbf{U}\omega)=\nabla\left[\left(\mu+\frac{\mu_t}{\sigma_{\omega 3}}\right)\nabla\omega\right]+(1-F_1)2\rho\frac{1}{\sigma_{\omega 2}\omega}\nabla k\nabla\omega+\alpha_3\frac{\omega}{k}P_k-\beta_3\rho\omega^2\,. \tag{8}$$

The coefficients of the new model are a linear combination of the corresponding coefficients of the underlying models: $\phi_3=F_1\phi_1+(1-F_1)\phi_2$, where ϕ_1 represents constant in the original Wilcox k-ω model and ϕ_2 constant in its transformed k-ε model.

The SST model, used for DES formulation, accounts for the transport of the turbulent shear stress and gives highly accurate predictions of the onset and the amount of flow separation under adverse pressure gradients. The proper transport behavior can be obtained using the limiter to the formulation of the eddy-viscosity:

$$\nu_t=\frac{a_1 k}{\max(a_1\omega, S, F_2)}\,, \tag{9}$$

where $\nu_t=\mu_t/\rho$, constant $a_1=0{,}3$, S is an invariant measure of the strain rate and F_2 is blending function similar to F_1, which restricts the limiter to the wall boundary layer, as the underlying assumptions are not correct for free shear flows:

$$F_2=\tanh\left[\left[\max\left(\frac{2\sqrt{k}}{\beta'\omega y},\frac{500\nu}{y^2\omega}\right)\right]^2\right]$$

The blending functions are critical to the success of the method. Their formulation is based on the distance to the nearest surface and on the flow variables.

$$F_1=\tanh\left\{\left\{\min\left[\max\left(\frac{\sqrt{k}}{\beta'\omega y},\frac{500\nu}{y^2\omega}\right),\frac{4\rho k}{CD_{k\omega}\sigma_{\omega 2}y^2}\right]\right\}^4\right\} \tag{10}$$

where y is the distance to the nearest wall and ν is the kinematic viscosity and: $CD_{k\omega}=\max(2\rho\frac{1}{\sigma_{\omega 2}\omega}\nabla k\nabla\omega, 1\times10^{-10})$.

The full transition model is based on two transport equations, one for the intermittency and one for the transition onset criteria in terms of momentum thickness Reynolds number. The transport equation for the intermittency, γ, reads:

$$\frac{\partial(\rho\gamma)}{\partial t}+\nabla(\rho\mathbf{U}\gamma)=P_{\gamma 1}-E_{\gamma 1}+P_{\gamma 2}-E_{\gamma 2}+\nabla\left[\left(\mu+\frac{\mu_t}{\sigma_y}\right)\nabla\gamma\right]. \tag{11}$$

The transition sources are defined as follows: $P_{\gamma 1}=2F_{lenght}\rho S\left[\gamma F_{onset}\right]^{c_{\gamma 3}}$; $E_{\gamma 1}=P_{\gamma 1}\gamma$, where S is the strain rate magnitude, F_{lenght} is an empirical correlation that controls the length of the transition region. The destruction/relaminarization sources are defined as follows:

$$P_{\gamma 2}=\left(2c_{\gamma 1}\right)\rho\Omega\gamma F_{turb};\quad E_{\gamma 2}=c_{\gamma_2}P_{\gamma 2}\gamma$$

where Ω is the magnitude of vorticity rate. The transition onset is controlled by the following functions:

$$Re_v=\frac{\rho y^2 S}{\mu};\ R_T=\frac{\rho k}{\mu\omega};\ F_{onset1}=\frac{Re_v}{2.193Re_{\theta c}};\ F_{onset2}=\min\left(\max\left(F_{onset1},F_{onset1}^4\right),2.0\right);$$

$$F_{onset3}=\max\left(1-\left(\frac{R_T}{2.5}\right)^3,0\right);\ F_{onset}=\max\left(F_{onset2},F_{onset3},0\right);\ F_{turb}=e^{-\left(\frac{R_T}{4}\right)^4}.$$

$Re_{\theta c}$ is the critical Reynolds number where the intermittency first starts to increase in the boundary layer. This occurs upstream of the transition Reynolds number, $\tilde{Re}_{\theta t}$, and the difference between the two must be obtained from an empirical correlation. Both the F_{lenght} and $Re_{\theta c}$ correlations are functions of $\tilde{Re}_{\theta t}$.

The constants for the intermittency equation are: $c_{\gamma 1}=0.03;\ c_{\gamma 2}=50;\ c_{\gamma 3}=0.5;\ \sigma_y=1.0$.

The modification for separation-induced transition is:

$$\gamma_{sep}=\min\left(2\cdot\max\left[\left(\frac{Re_v}{3.235Re_{\theta c}}\right)-1,0\right]F_{reattach},2\right);\quad F_{reattach}=e^{-\left(\frac{R_T}{20}\right)^4};\ \gamma_{eff}=\max\left(\gamma,\gamma_{sep}\right);$$

The transport equation for the transition momentum thickness Reynolds number, $\tilde{Re}_{\theta t}$, reads:

$$\frac{\partial\left(\rho\tilde{Re}_{\theta t}\right)}{\partial t}+\nabla\left(\rho\mathbf{U}\tilde{Re}_{\theta t}\right)=P_{\theta t}+\nabla\left[\sigma_{\theta t}\left(\mu+\mu_t\right)\nabla\tilde{Re}_{\theta t}\right]. \tag{12}$$

The source term is defined as follows:

$$P_{\theta t}=c_{\theta t}\frac{\rho}{t}\left(Re_{\theta t}-\tilde{Re}_{\theta t}\right)\left(1.0-F_{\theta t}\right);\ t=\frac{500\mu}{\rho U^2};$$

$$F_{\theta t}=\min\left(\max\left(F_{wake}e^{-\left(\frac{y}{\delta}\right)^4},1.0-\left(\frac{\gamma-1/50}{1.0-1/50}\right)^2\right),1.0\right),$$

$$\theta_{BL}=\frac{\tilde{R}e_{\theta t}\mu}{\rho U};\ \delta_{BL}=\frac{15}{2}\theta_{BL};\ \delta=\frac{50\Omega y}{U}\delta_{BL};\ Re_{\omega}=\frac{\rho\omega y^2}{\mu};\ F_{wake}=e^{-\left(\frac{Re_{\omega}}{10^5}\right)^2}.$$

The model constants for the $\tilde{R}e_{\theta t}$ equation are: $c_{\theta t}=0.03;\ \sigma_{\theta t}=2.0$.

The boundary condition for $\tilde{R}e_{\theta t}$ at a wall is zero flux. The boundary condition for $\tilde{R}e_{\theta t}$ at an inlet should be calculated from the empirical correlation based on the inlet turbulence intensity. The model contains three empirical correlations and the $Re_{\theta t}$ is the transition onset as observed in experiments.

The transition model interacts with the SST turbulence model, as follows:

$$\left.\begin{aligned}&\frac{\partial(\rho k)}{\partial t}+\nabla(\rho\mathbf{U}k)=\tilde{P}_k-\tilde{D}_k+\nabla\left[(\mu+\sigma_k\mu_t)\nabla k\right]\\&\tilde{P}_k=\gamma_{eff}P_k;\ \tilde{D}_k=\min\left(\max\left(\gamma_{eff},0.1\right),1.0\right)D_k\\&R_y=\frac{\rho y\sqrt{k}}{\mu};\ F_3=e^{-\left(\frac{R_y}{120}\right)^8};\ F_1=\max\left(F_{1orig},F_3\right);\end{aligned}\right\}\qquad(13)$$

where P_k and D_k are the original production and destruction terms for the SST model and F_{1orig} is the original SST blending function. The production term in the ω-equation is not modified.

Detached Eddy Simulation method (DES) is hybrid method, which combines characteristics of RANS simulations with elements of Large Eddy Simulation (LES), in order to predict turbulent fluid flow in highly separated regions, such existed around the bluff bodies.

The formulation of the DES-limiter function for the model, that prevent the model from switching to the LES model where the RANS model should be active (especially in the near wall domains, is:

$$F_{DES}=\frac{1}{1-(1-F_d)\max\left(1-C_{DES}\Delta\beta\frac{\omega}{\sqrt{k}},0\right)},\qquad(14)$$

where, $F_d=\tanh\left(\frac{8(\nu+\nu_t)}{\sqrt{U_{i,j}U_{i,j}k^2d^2}}\right)$ and $C_{DES}=0,61$.

DES simulation model uses a turbulence length scale obtained from the Menter's SST model's equations and compares it with the grid length scale to switch between LES and RANS. DES also demands complete simulation domain (due to not symmetric turbulent structures) and for DES initialization is used a converged RANS solution (here BSL solution).

3. The comparison of numerical and experimental results

The comparisons between the models serve to evaluate the capability of these models to resolve features of the flow accurately. According to Achenbach [1], this is the case of the turbulent flow with subcritical region ($Re<3\times10^5$). The comparisons of numerical and experimental results are shown in Fig.4, in the form of velocity distribution diagram, for several cross-section of quadratic duct.

By comparing experimental measurements and numerical simulation results it was obtained a validation of numerical method. It was clearly noticeable that the best velocity profile prediction was made by using BSL turbulence model [18]. The k-ε turbulence model shows the largest deviation of velocity, giving much smaller velocity values especially in the area of vortex shedding. Hence the k-ε turbulence model is proven to be unsuitable for flows with boundary layer separation and flows over curved surfaces. Both k-ε and k-ω turbulence models obtain lack of prediction in the area of vortex shedding. The SST turbulence model showed better velocity field prediction than k-ε and k-ω models, but slightly coarser than BSL model.

In further numerical analysis, the BSL turbulence model results were used as initial results for transient DES model.

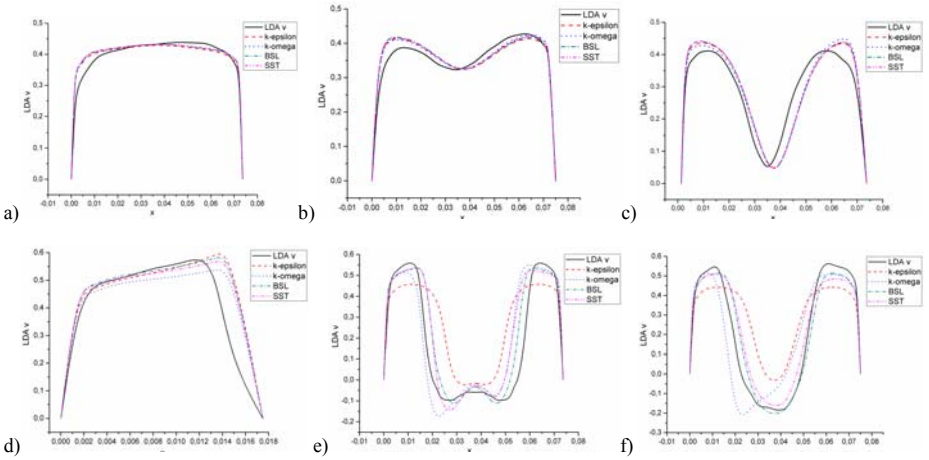

Figure 4. Comparison of velocity profiles: a) 6,5 cm in front of the sphere axis; b) 3 cm in front of the sphere axis; c) right in front of the sphere; d) in the sphere axis; e) right behind the sphere; f) 3 cm behind the sphere axis;

4. Results of numerical simulation for different duct cross-section range

After validation of numerical results, it was possible to investigate different duct cross-section cases, in order to determine the influence of the duct size to the flow characteristics around the smooth sphere. The main aim was to determine the critical ratio of the sphere diameter and cross section size, which could be considered as a limit up to which there is no substantial effect of the channel walls to the flow characteristics around the sphere. Also was determined the pressure coefficient (c_p) around the smooth sphere, and compared to the already known data. Finally, it was determined the separation point, which was also compared to the previously published data.|

Using RANS simulations it was investigated 6 different duct cross-section sizes (50mm, 75mm, 100mm, 150mm and 300mm), where the duct length was 300mm. Therefore a/d

ratio is: 1,25; 1,875; 2,5; 3,75 and 7,5, where: a – length of quadratic duct side and d – sphere diameter.
In the Fig. 5 is showed a graph of pressure coefficient c_p. The duct cross-section influence is obviously very strong for small sizes duct cross-sections, i.e. small a/d ratio. For duct cross-section size equal and larger than 150x150mm, there is not significant difference of pressure coefficient. Therefore for a/d $\geq$3,75 , there is inconsiderable duct cross-section influence on the flow around a smooth sphere.

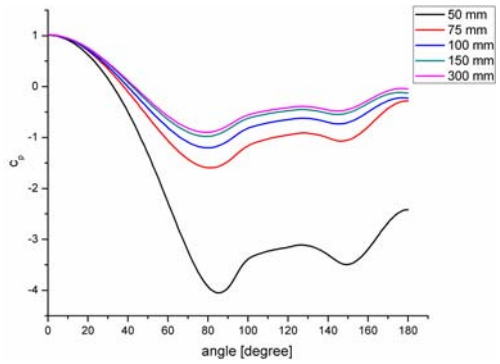

Figure 5. Comparison of coefficient c_p for different quadratic duct sizes obtained using RANS simulation.

In Fig.6 are shown shear stress diagram for different duct cross-sections, indicates the different value of separation point for different cross-section sizes. Using RANS simulations it is obtained that the separation angle slightly differs between observed cases, from 88,2 degrees for the duct cross-section 300x300 mm up to 89,7 degrees for the duct cross-section size 50x50 mm. For duct sizes 150x150 mm and 300x300 mm it is noticable that flow sepatation occures at almost the same sphere angle.

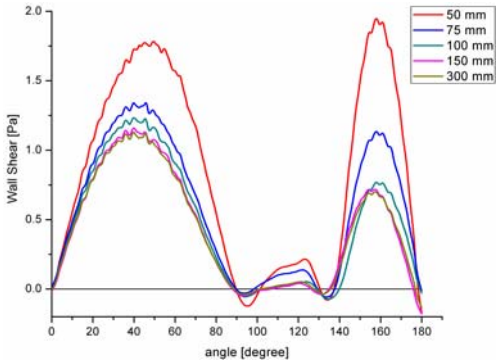

Figure 6. Comparison of shear stress graphs for different quadratic duct sizes (RANS).

For all cases, Reynolds number differs form $3 \cdot 10^4$ (50 mm cross-section) to $1{,}5 \cdot 10^4$.
The average y^+ values at near-wall nodes in the area of separation point are $y^+<1$, for all discretization meshes, which provides sufficient number of prismatic elements in boundary

layer around the smooth sphere. In order to obtain satisfactory numerical results this requirement must be satisfied [19].
Velocity vector field, for three different cross section ducts (75 mm, 150 mm and 300 mm) is shown in fig.7 and pressure gradient in Fig.8.

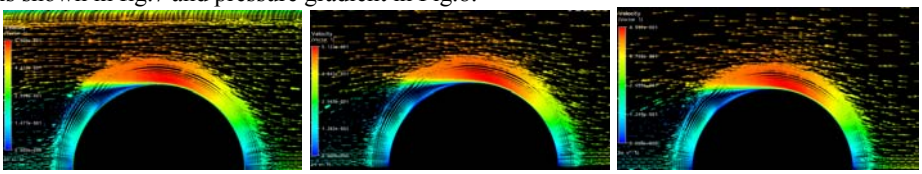

Figure 7. Velocity vector field for quadratic duct cross-sections: 75 mm, 150 mm and 300 mm.

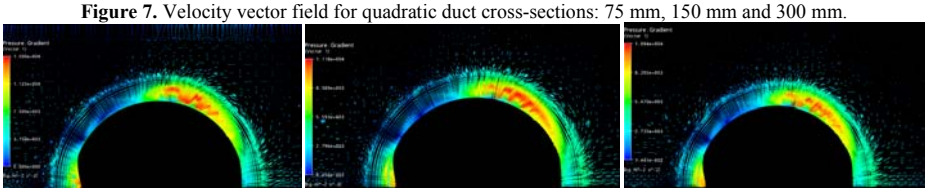

Figure 8. Pressure gradient around the sphere in quadratic duct cross-sections: 75 mm, 150 mm and 300 mm.

Pressure gradient increases along the sphere in the boundary layer and just before the separation point became positive (unfavorable), as it is represented in Fig.8.

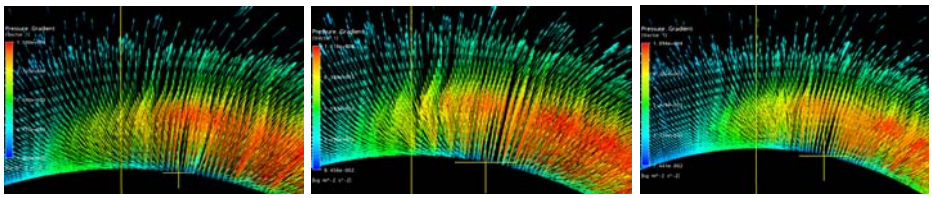

Figure 9. Pressure gradient in the area of flow separation for duct cross-section size:75 mm, 150 mm and 300 mm.

Detached Eddy Simulation requires the entire model geometry. Mesh elements around the sphere are the same size as for RANS simulations, and elements in the quadratic ducts are slightly larger, due to computational resource limitation. The initial results are obtained by using BSL turbulence model. A DES simulation requires much larger computational time for obtaining transient results.
In Fig.10 and Fig.11 are represented diagrams of pressure coefficient and wall shear diagram for all investigated cases, obtained by DES simulations.

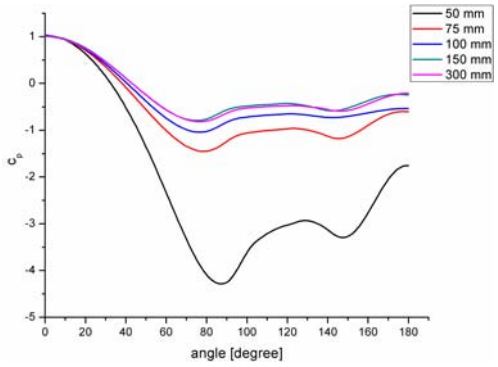

Figure 10. Comparison of coefficient c_p for different quadratic duct sizes obtained using DES simulation.

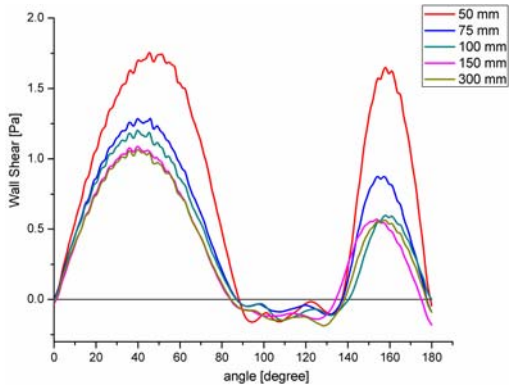

Figure 11. Comparison of shear stress graphs for different quadratic duct sizes (DES).

Using DES simulations it is obtained that the separation angle which varies from 84 degrees for the duct cross-section 300x300 mm up to 88,1 degrees for the duct cross-section size 50x50mm. DES simulation results always derive smaller sepatation angles than it is obtained using RANS simulations.

Detailed numerical simulations analysis of water flow around the smooth sphere in different quadratic cross-sections ducts indicate that separation flow occurs as it is represented in table I.

Duct size [mm]		50	75	100	150	300
	Re_{lok}	31367	20088	17842	16523	15821
RANS	ϕ_s	89,9	89,7	88,6	88,3	88,2
DES	ϕ_s	88,1	87,2	87	84,1	84

Obtained separation angles using DES simulations are in good agreement with those obtained by Constantinescu (84±1), for Reynolds number $1 \cdot 10^4$ [5]. Using FLUENT code and streamlines over the surface of the sphere from two different viewpoints, Jones and

Clarke [19] obtained slightly larger separation angle (88±1) and Achenbach [1] experimentally obtained slightly smaller separation angle (82±1).
By increasing local Reynolds number up to the Reynolds number $3 \cdot 10^4$ (i.e. increasing local velocity around the sphere) the separation angle also increases.

5. Conclusion

LDA measurement and RANS and DES simulations have been performed of the flow around a sphere at Re~10^4. The most favorable agreement with experimental measurements is obtained in DES cases computed using upwind discretizations for the convective terms, which resolve reasonably well the shedding mechanisms in the detached shear layers. The influence of the channel is expressed as long as ratio between the height of the channel and the sphere diameter do not come up to the value of 3,75 when this influence became negligible. This effect is particularly prominent in the pressure coefficient, while the boundary layer separation delay is very small (about 1 to 2 degrees). Based on these results it is concluded that it is possible to perform experimental research in small dimension domains and then perform a comparison of the obtained results with the actual flow problems without error because the effect of channel walls is not transferred to the flowed body.

Acknowledgement. This paper is supported by the Serbian Ministry of Sciences and Technological development (Project No. TR 33040; The revitalization of existing and designing of new micro and mini hydro power plants on the territory of south and southeastern Serbia).

References

[1] Achenbach E., (1972) Experiments on the flow past spheres at very high Reynolds numbers, *Journal of Fluid Mechanics*, **54** (3), pp. 565-575.
[2] Taneda S., (1956) Experimental Investigation of the Wake behind a Sphere at Low Reynolds Numbers, *Journal of Physics Society of Japan,* **11** (10), pp. 1104-1108.
[3] Taneda S., (1978) Visual observations of the flow past a sphere at Reynolds numbers between 104 and 106. *Journal of Fluid Mechanics*, **85**, 187-192.
[4] Bakic V., (2002) Experimental investigation of turbulent flows around a sphere, Ph.D. thesis, TUHH Hamburg, Germany.
[5] Constantinescu G., Squires K., (2004) Numerical investigations of flow over a sphere in the subcritical and supercritical regimes, *Physics of Fluids*, **16** (5). pp.1449-1466.
[6] Johnson T.A., Patel, V.C., (1999), Flow past a sphere up to a Reynolds number of 300", *Journal of Fluid Mechanics,* **378**, pp. 19-70.
[7] Mittal R., (1999) Planar Symmetry in the Unsteady Wake of a Sphere, *AIAA Journal*, **37**, pp. 388-390.
[8] Orszag S.A., Tomboulides A.G., (2000), Numerical investigation of transitional and weak turbulent flow past a sphere, *Journal of Fluid Mechanics*, **416**, pp. 45-73.
[9] Ploumhans P., Winckelmans G.S., Salmon J.K., Leonard A., Warren M.S. (2002) Vortex Methods for Direct Numerical Simulation of Three-Dimensional Bluff Body Flows: Application to the Sphere at Re=300, 500 and 1000", *Journal of Computational Physics*, **178**, pp. 427-463.
[10] Yun G., Kim D., Choi H., Vortical structures behind a sphere at subcritical Reynolds numbers, *Physics of Fluids* **18** (1). pp. 015102-015102-14.
[11] Durst F., Melling A., Whitelaw J.H., (1981) *Principles and practice of laser-doppler anemometry*, Academic Press Inc., London, New York.

[12] Durst F., Jovanovic J., Sender J., (1995) LDA measurements in the near-wall region of a turbulent pipe flow, *Journal of Fluid Mechanic*, **295**, pp. 305-335.
[13] Langtry R.B., Menter F.R., (2005) Transition Modeling for General CFD Applications in Aeronautics, *AIAA Journal*, **522**, pp. 1-14.
[14] Spalart P. R., Jou W.-H., Stretlets M., Allmaras S. R. (1997), Comments on the Feasibility of LES for Wings and on the Hybrid RANS/LES Approach, *Advances in DNS/LES, Proceedings of the First AFOSR International Conference on DNS/LES*
[15] Barth T.J., Jesperson D.C, (1989) The Design and Application of Upwind Schemes on Unstructured Meshes, *AIAA Journal*, **89**-0366, 1989.
[16] Wilcox D.C., (1986) Multiscale model for turbulent flows, *In AIAA 24th Aerospace Sciences Meeting.*.
[17] Menter F.R., (1994) Two-equation eddy-viscosity turbulence models for engineering applications, *AIAA-Journal.*, **32** (8), pp.1598–1605.
[18] Bogdanovic-Jovanovic J., Stamenkovic Z., Bogdanovic B., (2010) Numerical and experimental results of fluid velocity field around a smooth sphere using different turbulence models, *Proceedings of The international conference: Mechanical Engineering in XXI century*, pp. 103-106.
[19] Jones D.A., Clarke D.B., (2008) Simulation of Flow Past a Sphere using the Fluent Code, *Maritime Platforms Division, Defense Science and Technology Organization,* DSTO-TR-2232, Australia.

UNSTEADY TEMPERATURE MHD BOUNDARY LAYER ON THE POROUS BODY OF ARBITRARY SHAPE

Z. Boricic[1], D. Nikodijevic[2], Z. Stamenkovic[3]

[1]Faculty of Mechanical Engineering,
The University of Nis, Aleksandra Medvedeva 14, 18000 Nis
e-mail: zboricic@masfak.ni.ac.rs
[2] Faculty of Mechanical Engineering,
The University of Nis, Aleksandra Medvedeva 14, 18000 Nis
e-mail: dragisan@masfak.ni.ac.rs
[3] Faculty of Mechanical Engineering,
The University of Nis, Aleksandra Medvedeva 14, 18000 Nis
e-mail: zikas@masfak.ni.ac.rs

Abstract. The paper discusses the unsteady temperature two-dimensional laminar magnetohydrodynamic (MHD) boundary layer of incompressible fluid. Outer electric filed is neglected, magnetic Reynolds number is significantly lower then one i.e. considered problem is in induction-less approximation. Characteristic properties of fluid are constant and trough the body surface the same fluid as the fluid in primary flow has been injected (sucked). The boundary-layer equations are generalized such that the equations and the boundary conditions are independent of the particular conditions of the problem, and this form is considered as universal. Obtained universal equations are numerically solved using progonka method. Numerical results for the dimensionless velocity, temperature and friction factor in function of introduced sets of parameters are obtained, displayed graphically and used to carry out general conclusions about development of temperature MHD boundary layer.

1. Introduction

Idea of boundary layer control appear when Prandtl form the theory, and this idea came from Prandtl [1] himself. Boundary-layer control usually means either attempts to change the overall flow field to reduce pressure drag and/or to increase lift or attempts to control the position of boundary layer separation point. Since then, many passive and active techniques have been developed for the prevention or delay of flow separation: admit the body motion in streamwise direction, increasing the boundary layer velocity, boundary layer suction, second gas injection, profile laminarization, body cooling.

Interest in effect of outer magnetic filed on heat-physical processes appear fifty years ago [2]. A large number of theoretical investigations dealing with magnetohydrodynamic (MHD) flows of viscous fluids have been performed during the last decades due to their rapidly increasing applications in many fields of technology and engineering, such as MHD power generation, MHD flow meters, MHD pumps, magneto-biological and medical processes [3].

Many mathematic models have been proposed to explain the behaviors of the viscous MHD flow under different conditions. Generally, the fundamental equations governing the flow of a viscous electrically conducting fluid are very complicated in the form. Solutions of

mentioned models were followed with rapid increase of analytical papers and experimental procedures about heat transfer in MHD boundary layer [4-8].
In this paper for the sake of mentioned research richness, unsteady temperature two dimensional laminar MHD boundary layer of incompressible fluid on the porous surface body is considered. Externally applied magnetic field is still in relation to the fluid in outer flow and perpendicular to the body. Further on it is assumed there is no outer electric filed and magnetic Reynolds number is significantly lower then one i.e. considered problem is in induction-less approximation. Velocity of flow is considered much lower then speed of light and usual assumption in temperature boundary layer calculation that temperature difference is small (under 50^oC) is used, accordingly characteristic properties of fluid are constant (viscosity, thermal conductivity, electrical conductivity, magnetic permeability, mass heat capacity). Introduced assumptions simplify considered problem, however obtained physical model is interesting from practical point of view, because its relation with large number of MHD flows significant for technical practice. In described flow problem porous contour and externally applied magnetic field are used to control the flow in boundary layer. Partial differential equations, which mathematically describe considered problem, can be solved in every particular case using modern numerical methods.
In this paper quite different approach is showed based on ideas given in papers [9-11], which are extended in papers [12-14]. Essence of this approach is in introducing adequate transformations and sets of parameters in starting equations of laminar two-dimensional unsteady temperature MHD boundary layer of incompressible fluid on porous contour, which transform the equations system and corresponding boundary conditions into form unique for all particular problems and this form is considered as universal. Solution of universal equations obtained using modern numerical methods, can be on convenient wave saved and used for general conclusions derivation about developing of described temperature MHD boundary layer and for boundary layer calculation of observed problem special cases. Integration of obtained universal equations is performed once for all. In order to solve particular problems it is necessary to determine impulse equation using obtained universal solutions.

2. Mathematical analysis

Described two-dimensional problem of MHD unsteady temperature boundary layer in inductioneless approximation is mathematically presented with equation system:

$$\frac{\partial u}{\partial t}+u\frac{\partial u}{\partial x}+v\frac{\partial u}{\partial y}=\frac{\partial U}{\partial t}+U\frac{\partial U}{\partial x}+\nu\frac{\partial^2 u}{\partial y^2}-\frac{\sigma B^2}{\rho}\left(u-U\right); \tag{1}$$

$$\frac{\partial T}{\partial t}+u\frac{\partial T}{\partial x}+v\frac{\partial T}{\partial y}=\frac{\lambda}{\rho c_p}\frac{\partial^2 T}{\partial y^2}+\frac{\mu}{\rho c_p}\left(\frac{\partial u}{\partial y}\right)^2+\frac{\sigma B^2}{\rho c_p}\left(u-U\right)^2; \tag{2}$$

$$\frac{\partial u}{\partial x}+\frac{\partial v}{\partial y}=0; \tag{3}$$

and corresponding boundary and initial conditions:

$$u = 0, v = v_w(x,t), T = T_w \text{ for } y = 0; \tag{4}$$

$$u \to U(x,t), T \to T_\infty \text{ for } y \to \infty; \tag{5}$$

$$u = u_0(x,y), T = T_0(x,y) \text{ for } t = t_0; \tag{6}$$

$$u = u_1(t,y), T = T_1(t,y) \text{ for } x = x_0. \tag{7}$$

For further consideration velocity difference $v_1(x,y,t)$ and stream function $\Psi(x,y,t)$ are introduced with following relations:

$$v_1 = v - v_w, \frac{\partial \Psi}{\partial x} = -v_1, \ \frac{\partial \Psi}{\partial y} = u; \tag{8}$$

which transform equations (1) and (2) into system:

$$\begin{aligned} &\frac{\partial^2 \Psi}{\partial t \partial y} + \frac{\partial \Psi}{\partial y}\frac{\partial^2 \Psi}{\partial x \partial y} + \left(v_w - \frac{\partial \Psi}{\partial x}\right)\frac{\partial^2 \Psi}{\partial y^2} = \\ &= \frac{\partial U}{\partial t} + U\frac{\partial U}{\partial x} + \nu\frac{\partial^3 \Psi}{\partial y^3} - \frac{\sigma B^2}{\rho}\left(\frac{\partial \Psi}{\partial y} - U\right); \end{aligned} \tag{9}$$

$$\begin{aligned} &\frac{\partial T}{\partial t} + \frac{\partial \Psi}{\partial y}\frac{\partial T}{\partial x} + \left(v_w - \frac{\partial \Psi}{\partial x}\right)\frac{\partial T}{\partial y} = \\ &= \frac{\lambda}{\rho c_p}\frac{\partial^2 T}{\partial y^2} + \frac{\mu}{\rho c_p}\left(\frac{\partial^2 \Psi}{\partial y^2}\right)^2 + \frac{\sigma B^2}{\rho c_p}\left(\frac{\partial \Psi}{\partial y} - U\right)^2. \end{aligned} \tag{10}$$

Boundary and initial conditions are transformed into conditions:

$$\Psi = 0, \frac{\partial \Psi}{\partial y} = 0; \ T = T_w \text{ for } y = 0; \tag{11}$$

$$\frac{\partial \Psi}{\partial y} \to U(x,t); T \to T_\infty \text{ for } y \to \infty; \tag{12}$$

$$\frac{\partial \Psi}{\partial y} = u_0(x,y), T = T_0(x,y) \text{ for } t = t_0; \tag{13}$$

$$\frac{\partial \Psi}{\partial y} = u_1(t,y), T = T_1(t,y) \text{ for } x = x_0. \tag{14}$$

First equation of system (9) does not depend from second equation (10) and it can be solved independently. For solving of system second equation, solution of first equation is used.
For further consideration of described problem, new variables are introduced:

$$x = x,\ t = t,\ \eta = \frac{Dy}{h(x,t)};$$

$$\Phi(x,t,\eta) = \frac{D\Psi(x,y,t)}{U(x,t)h(x,t)};\ \Theta(x,t,\eta) = \frac{T_w - T}{T_w - T_\infty}; \tag{15}$$

where D is normalizing constant, and $h(x,t)$ is characteristic linear scale of transversal coordinate in boundary layer. According to introduced variables, system of equations (9-10) is transformed in new form:

$$D^2\frac{\partial^3\Phi}{\partial\eta^3} + f_{1,0}\left(\Phi\frac{\partial^2\Phi}{\partial\eta^2} - \left(\frac{\partial\Phi}{\partial\eta}\right)^2 + 1\right) + \left(f_{0,1} + g_{1,0}\right)\left(1 - \frac{\partial\Phi}{\partial\eta}\right) + \\ + \frac{1}{2}\left(F\Phi + \eta g\right)\frac{\partial^2\Phi}{\partial\eta^2} + D\lambda_{0,0}\frac{\partial^2\Phi}{\partial\eta^2} = z\frac{\partial^2\Phi}{\partial t\partial\eta} + UzX(\eta;x); \tag{16}$$

$$\frac{D^2}{P_r}\frac{\partial^2\Theta}{\partial\eta^2} - D^2E_c\left(\frac{\partial^2\Phi}{\partial\eta^2}\right)^2 - E_c g_{1,0}\left(1 - \frac{\partial\Phi}{\partial\eta}\right)^2 + \\ + \frac{1}{2}\left(F + 2f_{1,0}\right)\Phi\frac{\partial\Theta}{\partial\eta} + D\lambda_{0,0}\frac{\partial\Theta}{\partial\eta} + \frac{1}{2}\eta g\frac{\partial\Theta}{\partial\eta} = z\frac{\partial\Theta}{\partial t} - UzY(x;\eta); \tag{17}$$

where for the sake of shorter expression, the notations are introduced:

$$z = \frac{h^2}{\nu};\ g = \frac{\partial z}{\partial t};\ N = \frac{\sigma B^2}{\rho};\ g_{1,0} = Nz;\ F = U\frac{\partial z}{\partial x};$$

$$f_{1,0} = z\frac{\partial U}{\partial x};\ f_{0,1} = \frac{z}{U}\frac{\partial U}{\partial t};\ \lambda_{0,0} = -v_w\sqrt{\frac{z}{\nu}};$$

$Pr = \frac{\nu\rho c_p}{\lambda}$ - Prandtl number; $E_c = \frac{U^2}{c_p(T_w - T_\infty)}$ - Eckert number

$$X(x_1;x_2) = \frac{\partial\Phi}{\partial x_1}\frac{\partial^2\Phi}{\partial\eta\partial x_2} - \frac{\partial\Phi}{\partial x_2}\frac{\partial^2\Phi}{\partial x_1\partial\eta};\ Y(x_1;x_2) = \frac{\partial\Phi}{\partial x_1}\frac{\partial\Theta}{\partial x_2} - \frac{\partial\Phi}{\partial x_2}\frac{\partial\Theta}{\partial x_1}. \tag{18}$$

Now we introduce sets of parameters:

$$f_{k,n} = U^{k-1}\frac{\partial^{k+n}U}{\partial x^k\partial t^n}z^{k+n}\quad (k,n = 0,1,2,\ldots;k \vee n \neq 0),$$

$$g_{k,n} = U^{k-1}\frac{\partial^{k-1+n}N}{\partial x^{k-1}\partial t^n}z^{k+n}\quad (k,n = 0,1,2,\ldots,;k \neq 0),$$

$$\lambda_{k,n} = -U^k \frac{\partial^{k+n} v_w}{\partial x^k \partial t^n} \frac{z^{k+n+\frac{1}{2}}}{\nu} \quad (k,n = 0,1,2,...,;), \tag{19}$$

and constant parameter:

$$g = \frac{\partial z}{\partial t} = const.; \tag{20}$$

which can have different values. It can be noticed that first parameters are given in the terms (18). Introduced sets of parameters reflect the nature of velocity change on outer edge of boundary layer, nature of injection (ejection) velocity, alteration characteristic of variable N and temperature change on body surface, and a part from that, in the integral form (by means of z and $\partial z / \partial t$) pre-history of flow in boundary layer.

Using, introduced sets of parameters (19) like new independent variables instead of x and t , and differentiating operators for x and t :

$$\frac{\partial}{\partial \varphi} = \sum_{\substack{k,n=0 \\ k \vee n \neq 0}}^{\infty} \frac{\partial f_{k,n}}{\partial \varphi} \frac{\partial}{\partial f_{k,n}} + \sum_{\substack{k=1 \\ n=0}}^{\infty} \frac{\partial g_{k,n}}{\partial \varphi} \frac{\partial}{\partial g_{k,n}} + \sum_{k,n=0}^{\infty} \frac{\partial \lambda_{k,n}}{\partial \varphi} \frac{\partial}{\partial \lambda_{k,n}}; \tag{21}$$

where $\varphi = x,t$; and parameter derivates along coordinate x and time t are obtained by differentiation of equations (19):

$$\frac{\partial f_{k,n}}{\partial x} = \frac{1}{Uz}\left\{(k-1) f_{1,0} f_{k,n} + (k+n) F f_{k,n} + f_{k+1,n}\right\} = \frac{1}{Uz} Q_{k,n},$$

$$\frac{\partial f_{k,n}}{\partial t} = \frac{1}{z}\left\{(k-1) f_{0,1} f_{k,n} + (k+n) g f_{k,n} + f_{k,n+1}\right\} = \frac{1}{z} E_{k,n},$$

$$\frac{\partial g_{k,n}}{\partial x} = \frac{1}{Uz}\left\{(k-1) f_{1,0} g_{k,n} + (k+n) F g_{k,n} + g_{k+1,n}\right\} = \frac{1}{Uz} K_{k,n},$$

$$\frac{\partial g_{k,n}}{\partial t} = \frac{1}{z}\left\{(k-1) f_{0,1} g_{k,n} + (k+n) g g_{k,n} + g_{k,n+1}\right\} = \frac{1}{z} L_{k,n},$$

$$\frac{\partial \lambda_{k,n}}{\partial x} = \frac{1}{Uz}\left\{k f_{1,0} \lambda_{k,n} + \left(k+n+\frac{1}{2}\right) F \lambda_{k,n} + \lambda_{k+1,n}\right\} = \frac{1}{Uz} R_{k,n},$$

$$\frac{\partial \lambda_{k,n}}{\partial t} = \frac{1}{z}\left\{k f_{0,1} \lambda_{k,n} + \left(k+n+\frac{1}{2}\right) g \lambda_{k,n} + \lambda_{k,n+1}\right\} = \frac{1}{z} S_{k,n}; \tag{22}$$

where $Q_{k,n}; E_{k,n}; K_{k,n}; L_{k,n}; R_{k,n}; S_{k,n}$ are terms in curly brackets in obtained equations. It is important to notice that $Q_{k,n}; K_{k,n}; R_{k,n}$ beside the parameters depend on value $U \partial z / \partial x = F$. Using parameters (19), operators (21) and terms (22) system of equations (16-17) is transformed into equations:

$$\Im_1 = \sum_{\substack{k,n=0 \\ k \vee n \neq 0}}^{\infty} \left[E_{k,n} \frac{\partial^2 \Phi}{\partial \eta \partial f_{k,n}} + Q_{k,n} X\left(\eta; f_{k,n}\right) \right] +$$

$$+ \sum_{\substack{k=1 \\ n=0}}^{\infty} \left[L_{k,n} \frac{\partial^2 \Phi}{\partial \eta \partial g_{k,n}} + K_{k,n} X\left(\eta; g_{k,n}\right) \right] + \tag{23}$$

$$+ \sum_{k,n=0}^{\infty} \left[S_{k,n} \frac{\partial^2 \Phi}{\partial \eta \partial \lambda_{k,n}} + R_{k,n} X\left(\eta; \lambda_{k,n}\right) \right],$$

$$\Im_2 = \sum_{\substack{k,n=0 \\ k \vee n \neq 0}}^{\infty} \left[E_{k,n} \frac{\partial \Theta}{\partial f_{k,n}} + Q_{k,n} Y\left(\eta; f_{k,n}\right) \right] +$$

$$+ \sum_{\substack{k=1 \\ n=0}}^{\infty} \left[L_{k,n} \frac{\partial \Theta}{\partial g_{k,n}} + K_{k,n} Y\left(\eta; g_{k,n}\right) \right] + \tag{24}$$

$$+ \sum_{k,n=0}^{\infty} \left[S_{k,n} \frac{\partial \Theta}{\partial \lambda_{k,n}} + R_{k,n} Y\left(\eta; \lambda_{k,n}\right) \right];$$

where the following markings have been used for shorter statement: $\Im_1$ -left side of first equation of system (16), $\Im_2$ - left side of second system of equation (17).

In order to make Eqs. (23-24) universal it is necessary to show that value F can be expressed by means of introduced parameters. In order to prove mentioned we start from impulse equation of described problem:

$$\frac{\partial}{\partial t}\left(U\delta^*\right) + \frac{\partial}{\partial x}\left(U^2\delta^{**}\right) + U\left(\frac{\partial U}{\partial x} + N\right)\delta^* - \nu_w U - \frac{\tau_w}{\rho} = 0; \tag{25}$$

where:

$$\delta^*\left(x,t\right) = \int_0^{\infty}\left(1 - \frac{u}{U}\right)dy \text{ -displacement thickness;} \tag{26}$$

$$\delta^{**}\left(x,t\right) = \int_0^{\infty}\frac{u}{U}\left(1 - \frac{u}{U}\right)dy \text{ -momentum thickness;} \tag{27}$$

$$\tau_w\left(x,t\right) = \mu\left(\frac{\partial u}{\partial y}\right)_{y=0} \text{ -friction stress on the body.} \tag{28}$$

Introducing dimensionless characteristic functions:

$$H^*(x,t)=\frac{\delta^*}{h},\ H^{**}(x,t)=\frac{\delta^{**}}{h},\ \xi(x,t)=\frac{\tau_w h}{\mu U};\tag{29}$$

which, according to Eqs. (15), (26), (27) and (28), can be expressed in the following form:

$$H^*(x,t)=\frac{1}{D}\int_0^\infty\left(1-\frac{\partial\Phi}{\partial\eta}\right)d\eta,\quad H^{**}(x,t)=\frac{1}{D}\int_0^\infty\frac{\partial\Phi}{\partial\eta}\left(1-\frac{\partial\Phi}{\partial\eta}\right)d\eta,$$

$$\xi(x,t)=D^2\frac{\partial^2\Phi}{\partial\eta^2}|_{\eta=0}\,.\tag{30}$$

After transition to new independent variables (introduced parameters) in terms (30) values H^*, H^{**}, ξ become functions only from parameters $f_{k,n}$, $g_{k,n}$, $\lambda_{k,n}$ and g. Now, using parameters from impulse Eq. (25) after simple transformation next equation is obtained:

$$F=\frac{P}{Q};\tag{31}$$

where, for the sake of shorter expression following marks are used:

$$\begin{aligned}P=\xi-f_{1,0}\left(2H^{**}+H^*\right)-\left(f_{0,1}+g_{1,0}+\frac{1}{2}g\right)H^*-\lambda_{0,0}-\\-\sum_{\substack{k,n=0\\k\vee n\neq 0}}^{\infty}\left\{E_{k,n}\frac{\partial H^*}{\partial f_{k,n}}+\left[(k-1)f_{1,0}f_{k,n}+f_{k+1,n}\right]\frac{\partial H^{**}}{\partial f_{k,n}}\right\}\\-\sum_{k=1}^{\infty}\left\{L_{k,n}\frac{\partial H^*}{\partial g_{k,n}}+\left[(k-1)f_{1,0}g_{k,n}+g_{k+1,n}\right]\frac{\partial H^{**}}{\partial g_{k,n}}\right\}-\\-\sum_{k,n=0}^{\infty}\left\{S_{k,n}\frac{\partial H^*}{\partial\lambda_{k,n}}+\left[kf_{1,0}\lambda_{k,n}+\lambda_{k+1,n}\right]\frac{\partial H^{**}}{\partial g_{k,n}}\right\},\end{aligned}\tag{32}$$

$$\begin{aligned}Q=\frac{1}{2}H^{**}+\sum_{\substack{k,n=0\\k\vee n\neq 0}}^{\infty}(k+n)f_{k,n}\frac{\partial H^{**}}{\partial f_{k,n}}+\\+\sum_{\substack{k=1\\n=0}}^{\infty}(k+n)g_{k,n}\frac{\partial H^{**}}{\partial g_{k,n}}+\sum_{k,n=0}^{\infty}\left(k+n+\frac{1}{2}\right)\lambda_{k,n}\frac{\partial H^{**}}{\partial\lambda_{k,n}}.\end{aligned}\tag{33}$$

Last two equations define function F in terms of values, which depends only from introduced parameters. Equation system (23-24) is now universal system of equations of described problem. Boundary conditions, also universal, are given with terms:

$$\Phi = 0, \frac{\partial \Phi}{\partial \eta} = 0, \Theta = 0 \text{ for } \eta = 0; \quad \Phi \to 1, \Theta \to 1 \text{ for } \eta \to \infty,$$

$$\Phi = \Phi_0(\eta), \Theta = \Theta_0(\eta) \text{ for} \begin{Bmatrix} f_{k,n} = 0 \left(k, n = 0,1,2,..., k \vee n \neq 0\right) \\ g_{k,n} = 0 \left(k, n = 0,1,2,..., k \neq 0\right) \\ \lambda_{k,n} = 0 \left(k, n = 0,1,2,...\right) \\ g = 0 \end{Bmatrix}; \qquad (34)$$

where $\Phi_0(\eta)$ -Blasius solution for stationary boundary layer on the plate and $\Theta_0(\eta)$ is solution of following equation:

$$\frac{D^2}{P_r}\frac{d^2\Theta_0}{d\eta^2} - D^2 E_c \left(\frac{d^2\Phi_0}{d\eta^2}\right)^2 + \frac{\xi_0}{H^{**}}\Phi_0 \frac{d\Theta_0}{d\eta} = 0. \qquad (35)$$

Universal system of equations (23-24) with boundary conditions (34) are strictly for wide class of problems in which $z = At + C(x)$, where A is arbitrary constant and $C(x)$ some function of longitudinal coordinate. For other problems this equations are approximated universal equations.

Equation system (23-24) can be integrated in m-parametric approximation once for good and all. Obtained characteristic values can be used to yield general conclusions about development of described boundary layer and to solve any particular problem.

Before integration for scale of transversal coordinate in boundary layer $h(x,t)$ some characteristic value is chosen. In this case $h = \delta^{**}$ and accordingly to Eq. (30) $H^{**} = 1$, $H^* = \delta^* / \delta^{**} = H$, and equality (31) now have form:

$$F = 2\left[\xi - f_{1,0}(2+H) - \left(f_{0,1} + g_{1,0} + \frac{1}{2}g\right)H - \lambda_{0,0} - \right.$$
$$\left. - \sum_{\substack{k,n=0 \\ k \vee n \neq 0}}^{\infty} E_{k,n}\frac{\partial H}{\partial f_{k,n}} - \sum_{\substack{k=1 \\ n=0}}^{\infty} L_{k,n}\frac{\partial H}{\partial g_{k,n}} - \sum_{k,n=0}^{\infty} S_{k,n}\frac{\partial H}{\partial \lambda_{k,n}}\right]. \qquad (36)$$

Taking parameters $f_{k,n} = 0$, $g_{k,n} = 0$, $\lambda_{k,n} = 0, g = 0$ first equation of system (13) is simplified into form:

$$\frac{d^3\Phi_0}{d\eta^3} + \frac{\xi_0}{D^2}\Phi_0 \frac{d^2\Phi_0}{d\eta^2} = 0; \qquad (37)$$

and if $D^2 = \xi_0$ then previous equation became well-known Blasius equation. According to previous statement for normalizing constant D value 0,47 must be chosen. For selected value h equation (35) for determining variable Θ_0 became:

$$\frac{1}{P_r}\frac{d^2\Theta_0}{d\eta^2}+\Phi_0\frac{d\Theta_0}{d\eta}-E_c\left(\frac{d^2\Phi_0}{d\eta^2}\right)^2=0. \quad (38)$$

In this paper adequate approximations of system (23-24) is given in which influence of parameters $f_{1,0}$, $f_{0,1}$, $g_{1,0}$, $\lambda_{0,0}$ and g are detained and influence of parameter $f_{0,1}$ derivatives are disregarded. System (23-24) is simplified into following form:

$$\Im_1=Ff_{1,0}X\left(\eta;f_{1,0}\right)+gf_{1,0}\frac{\partial^2\Phi}{\partial\eta\partial f_{1,0}}+Fg_{1,0}X\left(\eta;g_{1,0}\right)+gg_{1,0}\frac{\partial^2\Phi}{\partial\eta\partial g_{1,0}} \quad (39)$$

$$\Im_2=Ff_{1,0}Y\left(\eta;f_{1,0}\right)+gf_{1,0}\frac{\partial\Theta}{\partial f_{1,0}}+Fg_{1,0}Y\left(\eta;g_{1,0}\right)+gg_{1,0}\frac{\partial\Theta}{\partial g_{1,0}}; \quad (40)$$

where function F in same approximation obtained from equation (36) have form:

$$F=2\left[\xi-f_{1,0}\left(2+H\right)-\left(f_{0,1}+g_{1,0}+\frac{1}{2}g\right)H-\lambda_{0,0}-gf_{1,0}\frac{\partial H}{\partial f_{1,0}}-gg_{1,0}\frac{\partial H}{\partial g_{1,0}}\right] \quad (41)$$

Boundary conditions, which coincide to equation system (39-40) are:

$$\Phi=0,\frac{\partial\Phi}{\partial\eta}=0,\Theta=0 \text{ for } \eta=0;\quad \Phi\to1,\Theta\to1 \text{ for } \eta\to\infty,$$

$$\Phi=\Phi_0\left(\eta\right),\Theta=\Theta_0\left(\eta\right) \text{ for } \left\{\begin{matrix} f_{1,0}=0,\ f_{0,1}=0,g_{1,0}=0 \\ \lambda_{0,0}=0,g=0 \end{matrix}\right\}; \quad (42)$$

which is obtained from condition (34), using same simplifications like for system of equations. Equations (39) and (40) are five-parametric once localized approximations of equations (23) and (24).

3. Results and discussion

In this section part of results obtained with numerical integration of universal equations (51) and (53) are given. All results are given for Prandtl number $Pr=6.99$, initial Eckert number $Ec=0.0005$ and constant parameter $g=0.05$.

Integration domain of the treated system is divided in two parts – first one from $f_{1,0}=0$ towards the stagnation point ($f_{1,0}>0$), and second one from $f_{1,0}=0$ towards the separation point ($f_{1,0}<0$). Discretisation of the equations was done applying implicit scheme, central for dimensionless transversal coordinate η and backward for $f_{1,0}$. As a result of such procedure, tridiagonal system of algebraic equations was obtained.

In both integration domains unsteadiness parameter $f_{0,1}$ takes positive or negative values corresponding to the accelerated or decelerated free stream, respectively. Magnetic

parameter $g_{1,0}$ starts from zero, corresponding to the absence of applied magnetic field, while parameter $\lambda_{0,0}$ reflects the suction (positive values) or blowing (negative values).

Figures 1 and 2 presents the variations of variables F, H and dimensionless shear stress ξ in function of dynamic parameter $f_{1,0}$ for different values of unsteadiness parameter $f_{0,1}$. It may be noted that accelerated free stream decrease the boundary layer thickness and increase the velocity gradient near the wall. Positive or unfavourable pressure gradients that decelerate the free stream ($f_{0,1} < 0$), increases boundary layer thickness and decrease the velocity gradient at the wall. Unfavourable pressure gradients can cause boundary layer separation, which often results in drastically altered flow patterns and losses. The shear stress at the wall is less downstream (to the separation point) than upstream, indicating that the wall shear stress decrease along the body. Obtained results indeed show that accelerated free stream ($f_{0,1} = 0.06$) moves boundary layer separation point ($\xi = 0$) downstream as expected, while deceleration have negative influence.

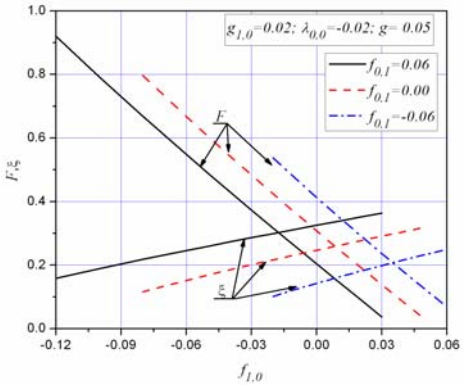

Figure 1. Function F and Dimensionless shear stress ξ for different values of unsteadiness parameter $f_{0,1}$

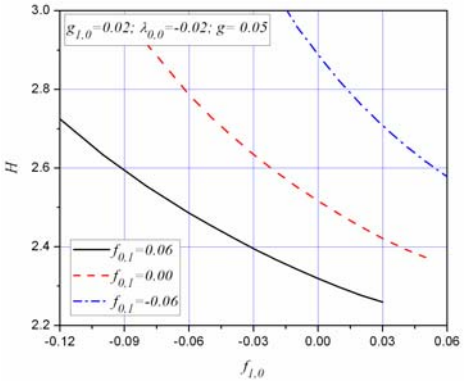

Figure 2. Function H for different values of unsteadiness parameter $f_{0,1}$

Figure 3 presents the variations of dimensionless temperature gradient ξ_t in function of dynamic parameter $f_{1,0}$ for different values of unsteadiness parameter $f_{0,1}$. Decelerated free stream cause the increase in heat transfer near the separation point while towards the stagnation point accelerated stream have same effect.

Figure 4 to 6 presents the influence of applied magnetic field on boundary layer characteristic functions. The effect of magnetic parameter $g_{1,0}$ on functions F, H and dimensionless shear stress ξ is shown in Figures 4 and 5. Figures present the case of decelerated outer flow ($f_{0,1} = -0.03$). It is interesting to note decreasing of functions F and H with increase of magnetic parameter and also with increase of dynamic parameter $f_{1,0}$. These results confirm the delay of the boundary-layer separation and greater postponement is achieved with increasing of magnetic parameter. Figures also show that increasing the magnetic filed decreases the velocity boundary layer thickness due to its damping effect.

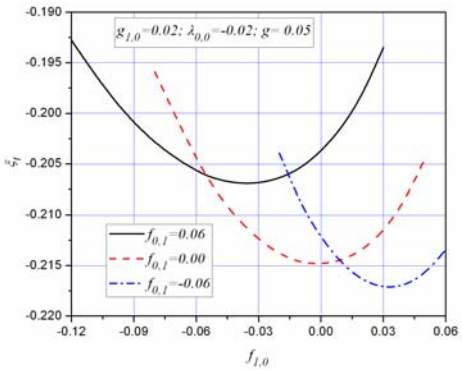

Figure 3. Dimensionless temperature gradient ξ_t in function of dynamic parameter for different values of unsteadiness parameter $f_{0,1}$

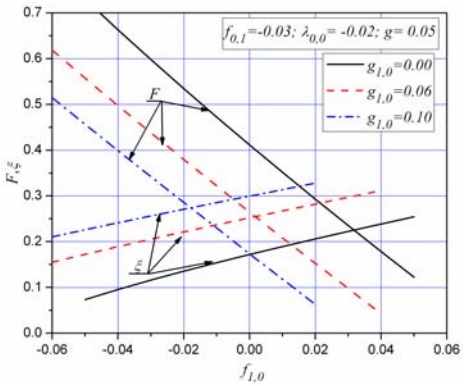

Figure 4. Function F and dimensionless shear stress ξ for different values of magnetic parameter $g_{1,0}$

From figure 4 also may be noted that with increase of magnetic parameter ξ also increase. This remark lead to conclusion that magnetic field postpone the boundary-layer separation and greater postponement is achieved with increasing of magnetic parameter $g_{1,0}$. Figure 4 is given for the case of decelerated outer flow ($f_{0,1} = -0.03$), however the same conclusion is obtained for the case of accelerated outer flow ($f_{0,1} > 0$).

The effect of magnetic parameter $g_{1,0}$ on dimensionless temperature gradient ξ_t in function of dynamic parameter $f_{1,0}$ is shown in the Figure 6. It is obvious that in the absence of the magnetic filed ($g_{1,0} = 0$) heat transfer increase forward to the separation point. In the vicinity of stagnation point magnetic filed increase the heat transfer.

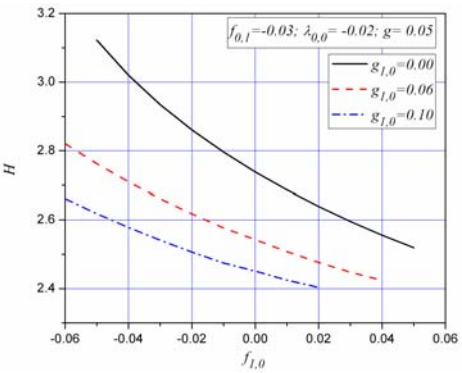

Figure 5. Function H for different values of magnetic parameter $g_{1,0}$

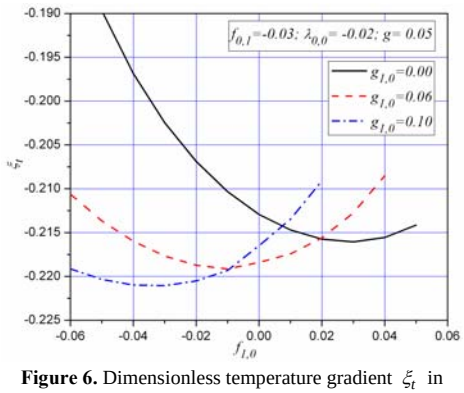

Figure 6. Dimensionless temperature gradient ξ_t in function of dynamic parameter for different values of magnetic parameter $g_{1,0}$

The effects of the suction or the blowing parameter $\lambda_{0,0}$ on the behaviors of the MHD boundary layer fluid flow are presented in Figs. 7 to 9. It is noticed that the blowing increases the boundary layer thickness and decreases the velocity gradient of flow. Nevertheless, the suction has the opposite effect on the boundary layer flow. All these results act in accord with the physical situations. Figure 9 shows that suction cause the increase in heat transfer while the blowing have the opposite effect.

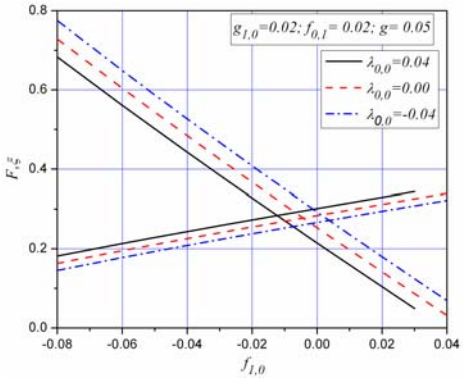

Figure 7. Function F and dimensionless shear stress ξ for different values of suction (blowing) parameter $\lambda_{0,0}$

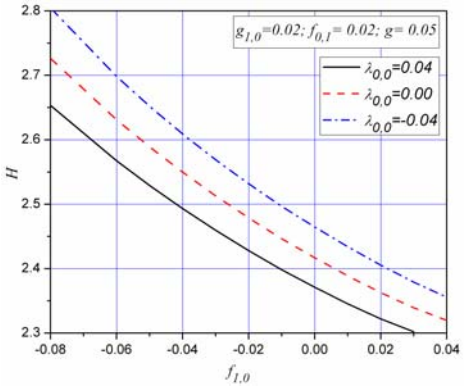

Figure 8. Function H for different values of suction (blowing) parameter $\lambda_{0,0}$

.

Dimensionless stream function Φ (dimensionless velocity) is given on Figure 10 for different values of unsteadiness parameter. It may be noted that velocity in boundary layer faster tends to the free stream velocity for the case of accelerated free stream and slower for the case of decelerated flow compared with steady outer flow ($f_{0,1} = 0$). Same conclusion is valid for other cross-sections of boundary-layer and for all values of dynamic and magnetic parameter.

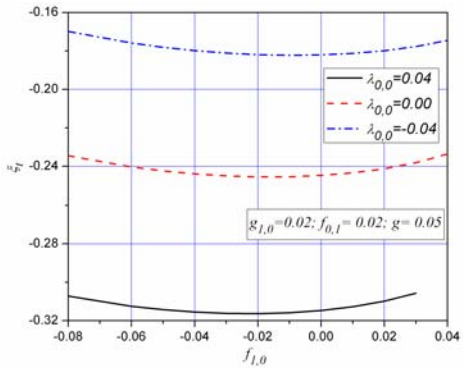

Figure 9. Dimensionless temperature gradient ξ_t in function of dynamic parameter for different values of suction (blowing) parameter $\lambda_{0,0}$

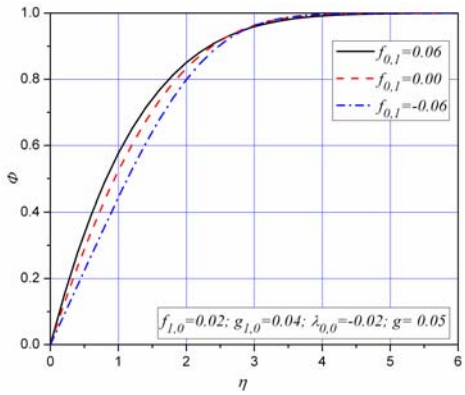

Figure 10. Effect of unsteadiness parameter $f_{0,1}$ on dimensionless velocity

Figure 11 shows the dimensionless stream function Φ in function of dimensionless transversal coordinate η for different values of magnetic parameter. From Figure 11, we observe that with increase of magnetic parameter this ratio also increase and the minimal value is obtained for the case of non-conducting fluid or for the case of magnetic field absence. This analysis indicates the significant influence of magnetic field on increasing velocity in boundary-layer. The results clearly show that the magnetic field tends to delay or prevent separation.

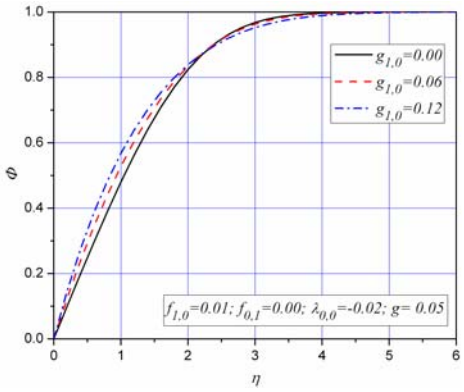

Figure 11. Effect of magnetic parameter $g_{1,0}$ on dimensionless velocity

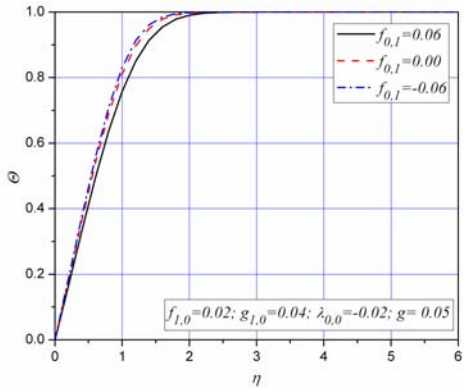

Figure 12. Effect of unsteadiness parameter $f_{0,1}$ on dimensionless temperature

It is interesting to note that the decelerated free stream increase the dimensionless boundary layer temperature, while the positive values of the same parameter have opposite effect as shown in the figure 12.

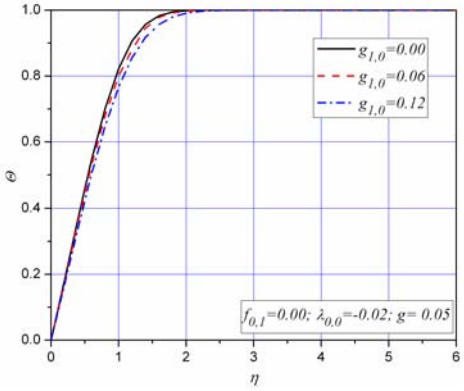

Figure 13. Effect of magnetic parameter $g_{1,0}$ on dimensionless temperatue

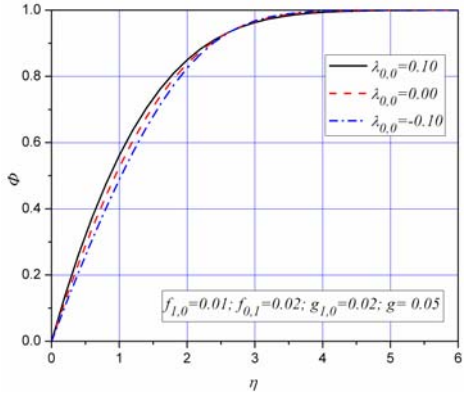

Figure 14. Effect of suction (blowing) parameter $\lambda_{0,0}$ on dimensionless velocity

In Figure 13, the effects of the magnetic parameter on the temperature profiles are shown. From this figure, it can be seen that the dimensionless temperature decreases (thermodynamic temperature increase) with the increase of magnetic parameter. It is

important to mention that obtained temperature function is not completely universal, since it depends on Prandtl number Pr .

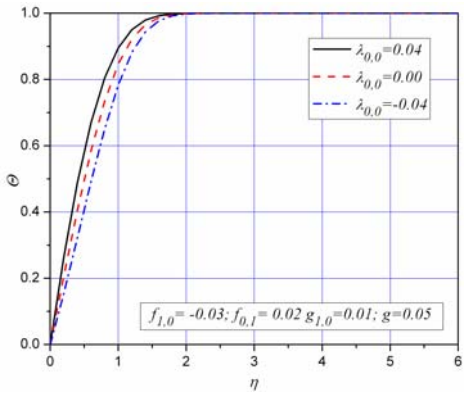

Figure 15. Effect of suction (blowing) parameter $\lambda_{0,0}$ on dimensionless temperature

The effects of the suction or the blowing parameter $\lambda_{0,0}$ on the dimensionless velocity and temperature in the MHD boundary layer are presented in Figures 14 and 15. It is noticed that the blowing decreases the velocity in the boundary layer while suction increase velocity and decrease the boundary layer thickness. As expected the suction tends to delay the boundary layer separation and have positive effects on the flow. All these results act in accord with the physical situations. The temperature distribution in function of dimensionless transversal coordinate η for different values of suction (blowing) parameter $\lambda_{0,0}$ is shown in Figure 15. Middle line presents the case of absence of suction or blowing. From this figure, it can be seen that the dimensionless temperature decreases (thermodynamic temperature increase) with the increase of blowing parameter.

4. Conclusion

The generalized similarity solution to the problem of the temperature two-dimensional MHD boundary layer flow on the porous body has been presented in this paper to exhibit the combined effects of the dynamic, magnetic and suction (blowing) parameters. This problem can be analyzed for every particular case i.e. for given function of free stream velocity and body temperature. Here is used quite different approach in order to use benefits of multi-parametric method and universal equations of observed problem are derived. These equations are solved numerically in some approximation and integration results are given in the form of diagrams and conclusions. The obtained results can be used in drawing about general conclusions of boundary-layer development and in calculation of particular problems as shown in the paper.

Acknowledgments

This paper is supported by the Serbian Ministry of Sciences and Technological development (Project No. TR 35016; Research of MHD flow in the channels, around the bodies and application in the development of the MHD pump).

References

[1] Schlichting H (1982), Grenzschicht-Theorie, Braun-Verlag, Karlsruhe.
[2] Blum E J and Mihailov J A (1966) Heat transfer in electroconductive fluid in presence of transversal magnetic field, Magnetohydrodynamics **5**, pp. 2-18.
[3] Molokov S., Moreau R. and Moffatt, H. (2007) Magnetohydrodynamics-Historical Evolution and Trends, Springer.
[4] Lu H Y and Lee C H (2009) Simulation of three-dimensional nonideal MHD flow at low magnetic Reynolds number, *Science China Series E-Technological Sciences*, **52**(12), pp. 3690-3697.
[5] Poggie J and Gaitonde D (2002) Magnetic control of flow past a blunt body: Numerical validation and exploration, *Physics of Fluids*, **14**(5), pp. 1720.1731.
[6] Abel M S and Nandeppanavar M M (2009) Heat transfer in MHD viscoelastic boundary layer flow over a stretching sheet with non-uniform heat source/sink, *Communications in Nonlinear Science and Numerical Simulation*, **14**(5), pp. 2120–2131.
[7] Ishak A, Nazar R, and Pop I (2009) MHD boundary-layer flow of a micropolar fluid past a wedge with constant wall heat flux, *Communications in Nonlinear Science and Numerical Simulation*, **14**(1), pp. 109–118.
[8] Abbas I A, Palani G, (2010) Effects of magnetohydrodynamic .ow past a vertical plate with variable surface temperature, *Applied Mathematics and Mechanics (English Edition)*, **31**(3), pp. 329.338.
[9] Loicijanski L G (1965) Universal equations and parametric approximations in theory of laminar boundary-layer, *AN SSSR Applied mathematics and mechanics*, **29**, pp. 70-87.
[10] Saljnikov V N (1978) A Contribution to Universal Solutions of the boundary-layer Theory, *Theoretical and Applied Mechanics*, **4**, pp.139-163.
[11] Busmarin O N and Saraev J V (1974), Parametric method in theory of unsteady boundary-layer, *Inz.-fiz. journal*, **XXVII**(1), pp. 110-118.
[12] Boricic Z, Nikodijevic D, Milenkovic D and Stamenkovic Z (2005) A form of MHD universal equations of unsteady incompressible .uid .ow with variable electroconductivity on heated moving plate, *Theoretical and Applied Mechanics*, **32**, pp. 65-77.
[13] Obrovic B, Nikodijevic D and Savic S (2009) Boundary-layer of dissociated gas on bodies of revolution of a porous contour, *Strojniski vestnik - Journal of Mechanical Engineering*, **55**(4), pp. 244–253.
[14] Nikodijevic D, Nikolic V, Stamenkovic Z and Boricic A (2011), Parametric method for unsteady two-dimensional MHD boundary-layer on a body for which temperature varies with time, Archives of Mechanics., **63**(1), pp. 57–76.

TURBULENT SWIRL FLOW DYNAMICS

Đ. Čantrak, M. Nedeljković and N. Janković

Faculty of Mechanical Engineering,
The University of Belgrade, Kraljice Marije 16, 11120 Belgrade 35
e-mail: djcantrak@mas.bg.ac.rs

Abstract. Turbulent swirl flow occurs in various technical systems and nature. Here are presented experimental results obtained in circular pipe behind axial fan as swirl generator for Reynolds number $2.36 \cdot 10^5$. Various experimental techniques were employed such as Laser Doppler Anemometry (LDA), Particle Image Velocimetry (PIV), original classical probes and smoke flow visualization with Nd:Yag laser. Each of techniques discovers turbulent swirl flow field characteristics in its own "point of view". LDA offers better insight into flow turbulence, but just for one velocity component and in one point. PIV offers good spatial overview (around 100mmx120mm) and averaged velocity field based on 300 pictures. Classical probes provided pressure distribution along the pipe diameter. Performed visualization gave better insight into fluid flow dynamics. Four characteristic flow regions in a cross section are obvious. Radial velocity distribution, documented by LDA and PIV, has shown that turbulent swirl flow must be accepted as three dimensional in the core region, what was neglected by classical probes. Flow integral characteristics calculated on the basis of all these methods have shown good agreement. Distinctions are the result of difference in velocity distribution in, especially, vortex core region.

Keywords: turbulence, swirl flow, LDA, PIV, classical probes, visualization.

1. Introduction

Study of swirl flows is of great significance in technical practice, as well as medicine and nature flows. Here are presented some results of study of turbulent swirl flow behind axial fan. Physical understanding of this phenomenon would enlighten many unsolved problems and help developing new turbulent numerical models for CFD analysis as their prediction requires rather sophisticated modeling. Turbulent swirl flow has been studied by various experimental techniques [1-9].

Velocity field was calculated from distribution of total and static pressures along a diameter obtain by classical probes, [5]. Correlation functions, probability distributions and statistical moments of the higher order, which are determined experimentally by the use of hot-wire anemometry, together with Particle Image Velocimetry (PIV) results, point out, very specific phenomena and transport processes in the core region and turbulent shear flow in pipe swirl flow [3,4,6-8].

In this test fan rotation speed was n=1500rpm and Reynolds number calculated on the basis of axial averaged velocity was $2.36 \cdot 10^5$. Two velocity component distributions, axial and circumferential are presented and compared for Laser Doppler Anemometry (LDA) and classical probe measurements. Distribution of time-averaged values obtained across the pipe section by these two techniques has shown very good agreement. On the basis of these results are calculated volume flow rate (Q), averaged axial velocity (U_m), average

circulation (Γ), swirl number (Ω), Reynolds number (Re), and other integral statistical characteristics of the turbulent swirl flow.
LDA measurements offer possibility to study turbulent statistical characteristics. In this way moments up to the fourth order have been calculated.
Flow visualization with Nd:Yag laser and smoke generator with paraffin oil was done in the cross and meridian pipe section.
The combination of these two techniques in two various pipe cross sections offer a possibility to prove swirl decay process, to achieve energy characteristics of the fans, as well as energy loss coefficient and etc. Turbulence interpretation and flow visualization investigated vortex core dynamics in generated turbulent swirl flow.
The presented results point out extraordinary complexity of the structure of generated three dimensional turbulent velocity fields.

2. Experimental Test Rig

Turbulent swirl flow in pipe was studied in the test rig presented in Fig. 1 on the fan's pressure side. Swirl generator is positioned at the pipe inlet, after the aerodynamically profiled free bell-mouth inlet for providing uniform flow at the fan inlet. Pipe inner diameter is D=0.4m, made of four sections of which two are transparent, one at the inlet 1.5m long and the second one at the outlet 1.38m long. Two nontransparent sections are 4m each long. Installation total length is L=27.35·D, with around 5mm wall thickness. LDA measurements were performed in transparent sections x=2.96·D and x=25.92·D from the test rig inlet. PIV measurements and flow visualization were performed in the same measuring section x=25.92·D. Measurements with classical probes were performed in section x=21.1·D.

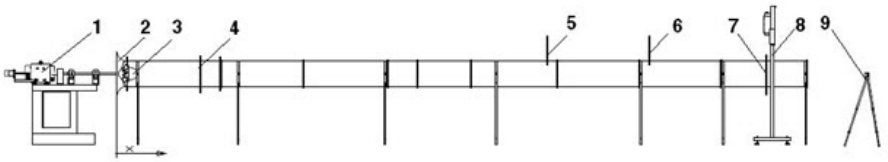

Figure 1. Experimental test rig: 1- DC motor with 5kW, 2- profiled free bell-mouth inlet, 3- axial fan (swirl generator), 4- LDA-1 measuring section, 5- smoke generator probe position, 6- classical probes position, 7- LDA-3 and PIV measuring section, flow visualization section, 8- Nd:Yag laser, 9- digital camera.

Fan rotation speed was regulated by a fully automated thyristor bridge with error up to ±0.5rpm. Axial fan has specific geometry (Fig. 2a.). External diameter of an axial rotor is 0.398m, while dimensionless ratio of hub and external diameter is 0.5. Impeller has nine blades with variable angle. In Fig. 2b is presented pipe coordinate system for cylindrical coordinates, used during tests.
Originally designed and manufactured axial fan (Fig. 2a.), has complex geometry and it was designed after the law of constant circulation $\Gamma=2\pi rW=const$. It is proved [5] that each produced swirl fluid flow decays, or transform itself, after some length in a pipe, into Rankine vortex. That is a reason why modeled axial fan with distribution of circumferential velocity component beyond the impeller is like in Rankine vortex. This was of great

importance for turbulent swirl flow studying, as the swirl type is known at the beginning of the test rig.

a) 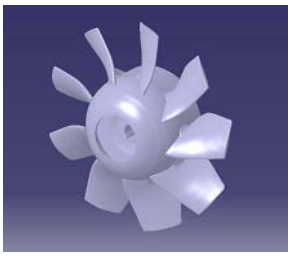 b) 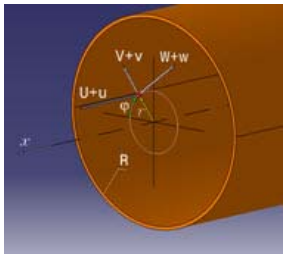

Figure 2. a) Modeled axial fan impeller geometry and b) used pipe coordinate system.

3. Experimental Investigation

3.1. PIV measurements

Stereo PIV measurements for other fan type and test rig configuration were earlier reported [1,2,4]. PIV measurements were performed in the section L=25.92·D in the middle of the pipe cross section, with region size 100x120mm (Fig. 1 and 3).

a) 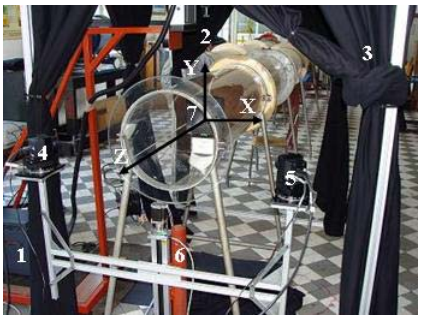

b) 

Figure 3. a) Stereo PIV configuration for calibration: 1- Nd:Yag laser power supply, 2- laser head, 3- chamber, 4- left camera, 5- right camera, 6- Π-shaped camera carrier with computer controlled linear guide, 7- target and b) and b) PIV seeding: 1- atomizer, 2- axial fan, 3- pipe, 4- measuring chamber.

Commercial stereo PIV system, made by TSI, was used. System consists of a dual head Nd:Yag laser (max power: 30mJ/pulse, wavelength 532nm, 15Hz), synchronization unit, adequate optics for the formation of the planar light sheet, two 12-bit CCD cameras with resolution of 1660x1200 pixels, 32fps. On the Nd:Yag laser was mounted cylindrical lens with focal length of -15mm and one spherical lens with focal length 500mm.
Stereo PIV measurements were conducted in pipe's cross-section, X-Y plane (Fig. 3a). In Fig. 3a is presented a stereo PIV configuration with two CCD cameras adjusted according to the Scheimpflug principle.

Laser sheet is approximately 1mm in width. The fluid flow is seeded with olive oil drops with average diameter 0.6μm and a reflection coefficient 1.47, generated by six-jet atomizer positioned at the axial fan free inlet (Fig. 3b).
Image processing has been performed by use of central difference image correction (CDIC) deformation algorithm in combination with FFT correlator (Fig. 4) [11,12]. This four-pass method employed an interrogation region of $32x32px^2$. The vector fields were validated using standard velocity range criteria and a 3x3 local median filter. Any missing vectors were interpolated using a 3x3 local mean technique. The number of interpolated vectors was, in average, around 6%.

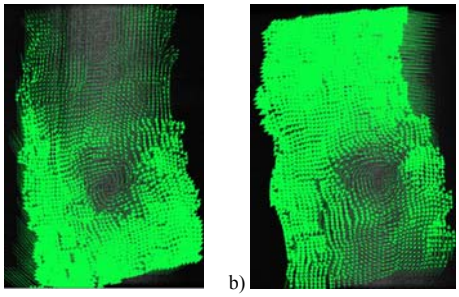

Figure 4. Data processing: a) left camera and b) right camera.

3.2. LDA measurements

LDA measurements have been carried out using one-component laser Doppler system in sections LDA-1 and LDA-3 (Fig. 1) along the vertical diameter on distance 10mm each. LDA system was model Flow Explorer Mini LDA, Dantec, with BSA F30 signal processor model. Measurement distance is at 285mm, power 35mW, measurement volume diameter 0.1mm, measurement volume length 1mm and maximum velocity 27m/s. It works in backscattered mode. Velocity was measured with uncertainty lower than 0.1%. Instantaneous velocities in the axial and radial directions have been measured at the same point by rotating the LDA optics for 90 degrees (Fig. 5a). Circumferential velocity component was measured from up and down side of the pipe (Fig. 5b).
Fog generator Hurricane 1700, Chauvet, and system of plastic pipes for accumulation and fog distribution were employed for flow seeding (Fig. 5c). HI TECH, JBSYSTEMS, liquid with eucalyptus extract, on water basis, was used. In this way enough seeding was obtained, which resulted with signal frequency in some positions more than 15 kHz. Seeding was naturally sucked in the test rig by the fan.

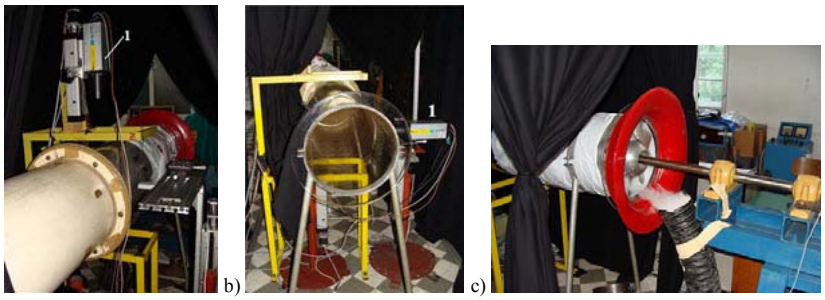

Figure 5. LDA measurements: a) circumferential velocity component, b) axial and radial velocity component and c) LDA seeding.

3.3. Measurements with original classical probes

Measurement method with original classical probes is previously described in details [13]. It is assumed for application of this measuring method that the flow is two-dimensional. Fig. 6a shows set-up for determination of time-averaged velocity vector. Afterwards in this position is placed a combined Prandtl probe to first determine total and later static pressure in the same point (Fig. 6b).

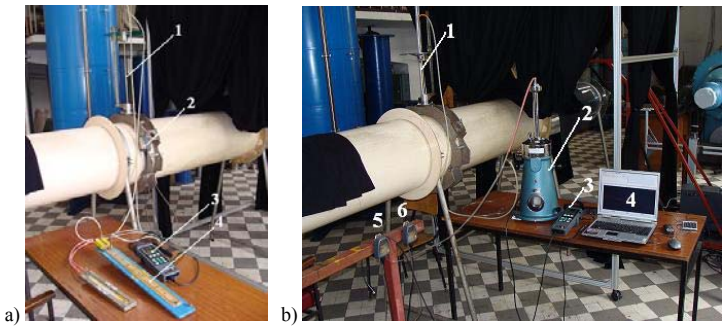

Figure 6. Measurements with classical probes: a) Determination of the averaged flow angle: 1- angle probe, 2- differential pressure transmitter (Δp=100Pa), 3- data logger, 4- U-pipe, b) Determination of the dynamic pressure: 1- modified Prandtl probe, 2- Betz micromanometer, 3- data logger, 4- lap top for data processing, 5- differential pressure transmitter (Δp=100Pa), 6-differential pressure transmitter (Δp=10hPa).

In order to define flow angle, two silicone hoses are connected, parallel, to the precise differential inclined U-type micro-manometer with alcohol and pressure transmitter for small pressures (Δp=100Pa, Testo model 0638.1347) with data logger Testo 400. Angle is investigated by rotating probe around its axis. The reading of this differential manometer equals zero, when the probe top is positioned in such a way that the probe is collinear with the averaged velocity vector.

Afterwards the combined Prandtl probe is positioned in this angle and the dynamic pressure is determined in two steps [13]. The probe is connected to the Betz micro-manometer, with an accuracy of 5 Pa, and parallel to one of differential pressure transmitters, Testo 0638.1347 (Δp=100Pa, accuracy ±0.3Pa±0.5% of reading, resolution 0.1Pa), Testo 0638.1447 (Δp=10hPa, accuracy ±0.03hPa, resolution 0.001hPa) or even in some cases

Testo 0638.1457 (Δp=100hPa, accuracy ±0.1hPa, till 20hPa, resolution 0.01hPa) depending on the measured pressure range. Air temperature and relative humidity were determined by use of Testo 450 with 0.1 resolution.

3.4. Flow visualization techniques

Flow visualization was performed in the pipe cross section and in meridian plane in section x=25.92·D. Illumination was Nd:Yag laser, λ=532nm, 30mJ/pulse, 15Hz, with mounted cylindrical lens f=25mm and one spherical lens f=500mm. Smoke generator (Elven, Precision Limited) probe has a Pitot-tube geometry with heater on the top. It was positioned upstream the measuring section as defined in Fig. 1. Used digital camera was SONY, DSC-H3, 10X Optical Zoom, F/3.5-4.4, 8.1MP with 30 fps and was positioned like in Fig. 1 or from a side.

4. Results and Analysis

4.1. Particle Image Velocimetry

Averaged velocity field based on 300 couples of images made in a sequence is presented in Fig. 7.

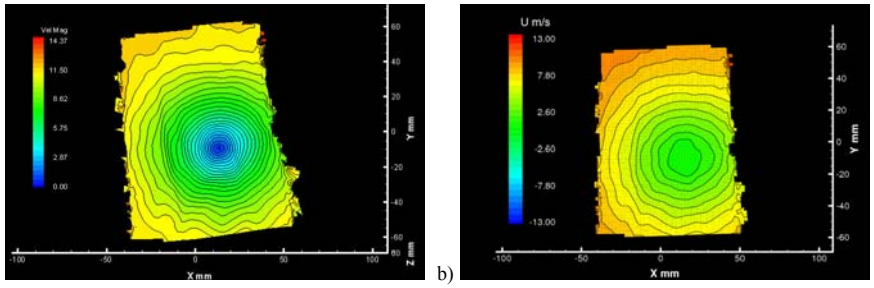

Figure 7. a) Averaged velocity field and b) Averaged axial velocity component field.

In this measuring section, for specified flow regime, can be concluded that even averaged velocity field is not axisymmetric.
Vortex core dynamics is given in the following pictures.

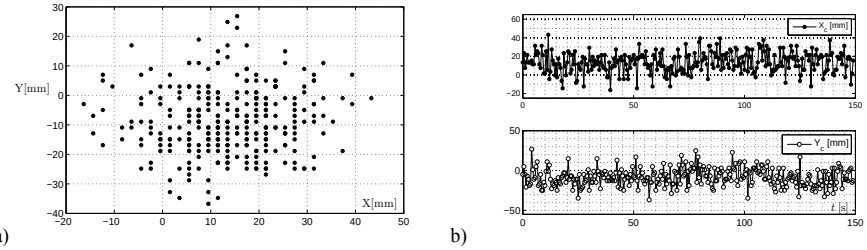

Figure 8. a) Coordinates of the vortex core center for 300 captures; b) Time dependence of the vortex core center coordinates during capture time.

These results prove great dynamics of the turbulent swirl flow.

4.2. LDA

Distribution of time averaged values of axial and circumferential velocity components are presented in Fig. 9. Indexes denote LDA measuring section.

Here four different zones in each cross section can be distinguished. In the center is vortex core where fluid rotates by the solid body law *W=r·const.*, what is obvious in Fig. 9b. In this zone even backflow may occur. Zone situated between the vortex core and the sound flow region is called shear layer.

Here is a big influence of inner viscosity caused by velocity gradients in radial direction and dominant turbulence intensity. Next zone is sound flow region. Here fluid rotates by optional law *W=f(r)*, of which here (Fig. 9b) is obeyed a law *W=const/r*, what was a design principle for this axial fan. In this zone axial velocity distribution is almost uniform. Boundary layer zone is the fourth one [3,8].

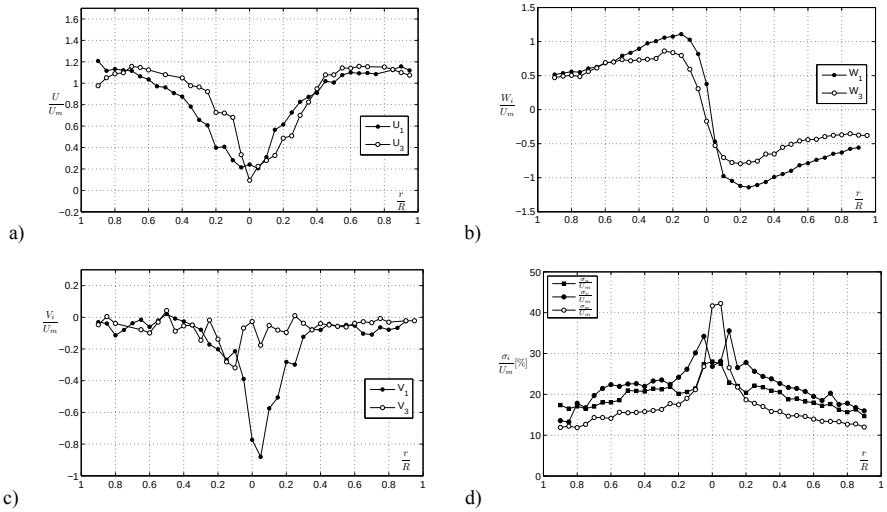

Figure 9. Distribution of the time averaged: a) axial, b) circumferential and c) radial velocity component along the vertical diameter; d) Distribution of turbulence intensity for section LDA-1.

Distribution of the radial velocity supports conclusions about non axisymmetric distribution presented in Figs. 7 and 8.

Turbulence intensities for section LDA-1 are given in the Fig. 9d. Turbulence intensity has great values for all three components in the whole region and especially in the vortex core what is also related to the vortex core dynamics.

Volume flow rate and averaged circulation are to be calculated on the basis of the following equations:

$$Q = 2\pi R^2 \int_0^1 kU\mathrm{d}k, \qquad \Gamma = 2\pi R \frac{\int_0^1 k^2 UW\mathrm{d}k}{\int_0^1 kU\mathrm{d}k}, \tag{1}$$

where $k=r/R$ is dimensionless radius. Volume flow rates calculated for sections LDA-1 and LDA-3 are Q_1=1.179m^3/s and Q_2=1.156m^3/s, where difference is around 1.95%. Non axisymmteric velocity distribution results in less then 3% difference in the volume flow calculation for one and other half of the pipe. Averaged axial velocities in both sections are $U_{m,1}$=9.38m/s and $U_{m,3}$=9.2m/s.

Averaged circulations are Γ_1=5.49m^2/s and Γ_3=4.79m^2/s. In this way swirl decay process is proved [5,9].

Non-dimensional swirl parameter (Ω) can be obtained in the following way:

$$\Omega=Q/(R\Gamma). \tag{2}$$

It has values Ω_1=1.1 and Ω_3=1.2.

Values of the normalized central moments for all three velocity components of the third S_i, and the fourth order F_i, where i= *u, v* and *w*, in section LDA-1 are given in Fig. 10.

They are defined in the following way:

$$S_i = \overline{u_i^3}\big/\sigma_i^3, \quad F_i = \overline{u_i^4}\big/\sigma_i^4, \tag{3}$$

where i stands for all three velocity components.

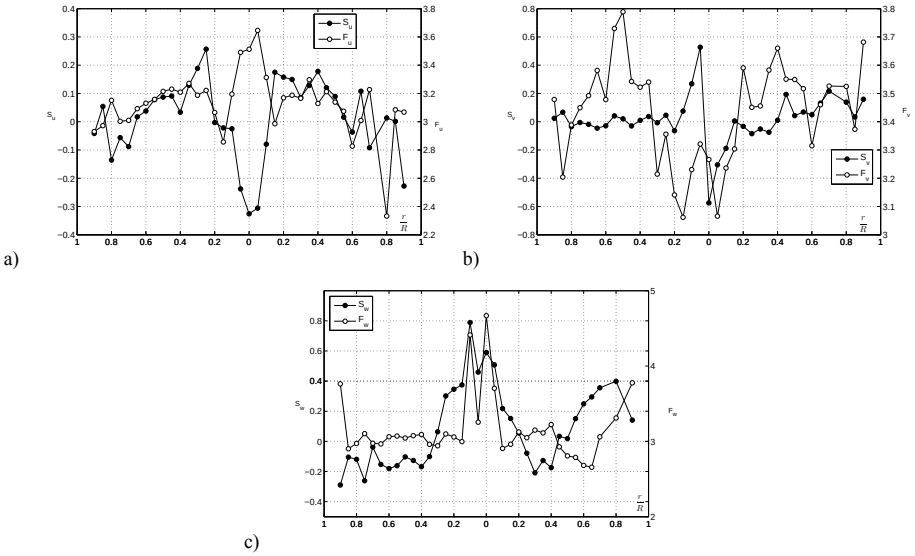

Figure 10. Skewness and flatness coefficients for a) axial, b) circumferential and c) radial velocity fluctuations in section LDA-1.

It is obvious that all skewness and flatness coefficients differ from adequate values for normal distribution 0 and 3, respectively. This is especially case in the vortex core region. It is obvious that in the vortex core and shear layer maximum F_u corresponds to minimum S_u.

This emphasizes presence of great negative fluctuations of axial velocities, but above all very frequent appearance of small fluctuations which are generated during movement of the turbulent swirls in the region of small spatial changes of the velocity field [6,7].
Acquisition time of 10s was set as stop criteria for all measurements. Data frequency very along the vertical diameter and also for measured velocity component. The data validation during test was in average 85%. Sensitivity was adjusted to the values 1200-1400V.

4.3. Original classical probes

Distribution of the relative static and total pressure is given in the Fig. 11. It looks almost symmetrical. It should have in mind that this experimental procedure considers no third velocity component and it is also measured in the longer period of time.

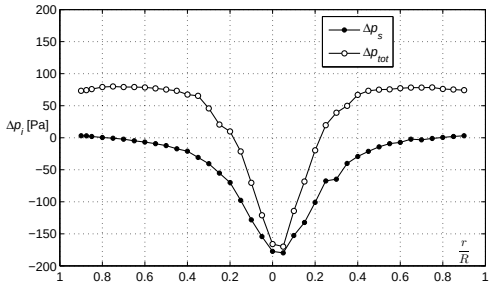

Figure 11. Total and static pressure distribution.

It should be pointed out that repeatability of the measured values is poor in the vortex region, like in the case of LDA measurements in this region.

4.4. Flow visualization

Various visualization methods have been used, like ones with filaments, stroboscope, speed camera with 1200 fps, ordinary digital camera, fog generators, and finally with Nd:Yag laser and fog generator with paraffin oil.
Images for these two planes are given in Fig. 12.

a) 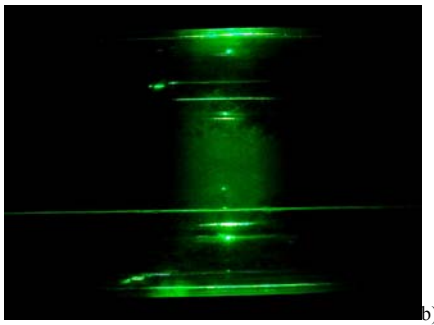 b) 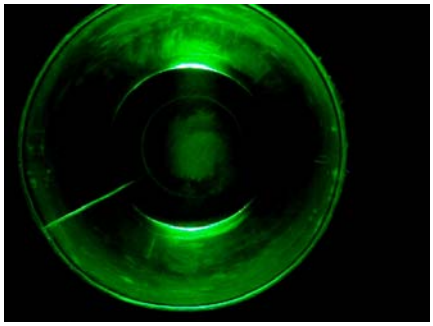

Figure 12. Flow visualization in a) meridian plane and b) cross-section. .

Very dynamic process is obvious.

5. Conclusions

Obtained measurements and visualization give closer insight into physics of complex flow processes in the swirl flow.

PIV measurements started revealing dynamics of the turbulent swirl flow. It was shown that, at least for this regime and with the help of used equipment, vortex center is out of the pipe center, even for the averaged value. However, this difference is not great. This pointed out nonaxisymmetric flow, what was also proved with radial component distribution.

This was also reason for differences in calculation of integral values in the case of LDA and classical probes use.

Statistical description of turbulence needs moments of the higher order as the values of skewness and flatness coefficients, especially for vortex and viscous region, differ from values for normal distribution.

These investigations offer much greater opportunities in investigation of turbulent swirl flow behind the axial fans and relating them to the axial fan characteristics.

More regimes and tested fans need to be processed in order to make definite conclusions about behaving of the turbulent swirl flows behind axial fans. Also PIV measurements in meridian section should be performed.

Better insight into these turbulent processes would give Time-resolved PIV as well as three-component LDA or Hot-wire anemometry measurements.

Performed and planned investigations will make possible, not just testing, but also development of new theoretical and numerical models for this class of very complex turbulent fluid flows.

Acknowledgement. This work was funded by grants from the Ministry of Science and Technological Development, Republic of Serbia Project TR 35046 and Bilateral Project with DAAD: Investigation of the Turbulent Structure behind the Axial Fan Impellers by Use of the HWA, LDA and PIV Measuring Techniques and CFD Analysis.

References

[1] Protić Z, Nedeljković M, Čantrak Đ, Janković N (2010) Novel Methods for Axial Fan Impeller Geometry Analysis and Experimental Investigations of the Generated Swirl Turbulent Flow, *Thermal Science*, Vol. 14, pp. S125-S139.

[2] Ilić J, Čantrak Đ, Srećković M (2007) Laser Sheet Scattering and the Cameras' Positions in Particle Image Velocimetry, *Acta Physica Polonica A*, Vol. 112, No 5., pp. 1113-1118.

[3] Čantrak S, Benišek M, Nedeljković M, Lečić M (2001) Problems of Non-Local Turbulent Transfer Modelling, *ZAMM*, Vol. 81, S4 (2001), pp. 913-914.

[4] Čantrak Đ, Ilić J, Hyde M, Čantrak S. et al., PIV Measurements and Statistical Analysis of the Turbulent Swirl Flow, *Proceedings of the ISFV 13 – 13th International Symposium on Flow Visualization, FLUVISU 12 – 12th French Congress on Visualization in Fluid Mechanics,* J Prenel and Y Bailly (Eds.), CD-ROM, ID 183-0804203.

[5] Benišek M (1979) *Investigation of the Turbulent Swirling Flows in Straight Pipes*, (in Serbian language), Ph. D. thesis, Faculty of Mechanical Engineering, University of Belgrade, Belgrade.

[6] Čantrak S (1981) *Experimental Investigation of the Statistical Properties of Swirling Flows in Pipes and Diffusers*, (in German language), Ph. D. thesis, Faculty of Mechanical Engineering, Technical University Karlsruhe, Karlsruhe.
[7] Lečić M. (2003) *Theoretical and Experimental Investigations of the Turbulent Swirling Flows*, (in Serbian language), Ph. D. thesis, Faculty of Mechanical Engineering, University of Belgrade, Belgrade.
[8] Čantrak S., Benišek M. (1982) Characteristic Magnitudes Determined from Mean Velocity Distributions of Turbulent Swirling Flow in Pipes, *ZAMM*, Vol. 62, Issue 4, pp. 201-203.
[9] Steenbergen W, Voskamp J (1998) The Rate of Decay of Swirl in Turbulent Pipe Flow, *Flow Measurement and Instrumentation*, Vol. 9, Issue 2, pp. 67-78.
[10] Ristić S (2007) Laser Doppler Anemometry and its Application in Wind Tunnel Tests, *Scientific Technical Review*, Vol. LVII, No.3-4, pp. 64-76.
[11] Wereley S, Gui L (2003) A Correlation-based Central Difference Image Correction (CDIC) Method and Application in a Four-roll Mill Flow PIV Measurement, *Experiments in Fluids*, Vol. 34, pp. 42-51.
[12] Adrian R (1997) Dynamic Ranges of Velocity and Spatial Resolution of Particle Image Velocimery, *Meas. Sci. Technol.*, Vol. 8, pp. 1393-1398.
[13] Benišek M, Lečić M, Ilić D, Čantrak Đ (2010) Aplication of New Classical Probes in Swirl Fluid Flow Measurements, *Experimental Techniques*, Vol. 34, Issue 3, pp. 74-81.

THE RESEARCH ON THE AERODYNAMIC COEFFICIENT EFFECTS ON THE STABILITY OF THE AXIS-SYMMETRICAL PROJECTILE

D. Jerkovic[1], S. Ilic[1], A. Kari[1], D. Regodic[2]

[1] Department of military mechanical engineering
Military academy, Pavla Jurisica Sturma 33, 11000 Belgrade
e-mail: damir.jerkovic@va.mod.gov.rs
e-mail: slobodan.ilic@va.mod.gov.rs
e-mail: aleksandar.kari@va.mod.gov.rs
[2] Faculty of Management,
Singidunum University, Bulevar Zorana Djindjica 44, 11000 Belgrade
e-mail: dregodic@singidunum.ac.rs

Abstract.

Theoretical and computational motion models of the classic axis-symmetrical projectile, through standard atmosphere, are presented in this paper. Physical and mathematical model of aerodynamic force and moment acting on classic symmetrical projectile is defined. Theoretical model of aerodynamic coefficients determination is described. Aerodynamic coefficients and derivatives of projectile model are calculated with adopted models of calculation. Aerodynamic coefficients as function of Mach numbers and angle of attack of projectile model are determined experimentally. The comparative analysis of experimental and calculated values of aerodynamic coefficients of projectile model is done. Those values are compared with appropriate values of aerodynamic coefficients of similar types of projectiles. Qualitative evaluation of calculated and experimental values of aerodynamic coefficients is created, and its results are used for the flight model of projectile with six degrees of freedom. Calculation of projectile path is used for the analysis of trajectory and motion stability of projectile model in the real atmosphere. Computational exterior ballistics program is used for determination of numerical and graphic comparison of path elements, stability parameters, and evaluation of precision measurement of classic axis-symmetrical projectile. Empirical evaluation and verification of aerodynamic coefficients calculations, in regard to experimental values, are done with six degrees of freedom calculation program model.

1. Introduction

The accuracy and precision of any mechanical system depend on a proper model and experimental results. The projectile as a mechanical system with its geometric and dynamic characteristics has to save energy during a flight through the atmosphere. The optimal – aerodynamic shape of the projectile provides stable flight, decreasing drag and preserving velocity.

A modern classic projectile is symmetric solid with front part – nose (shape of *ogive* or *paraboloid*), main cylindrical part (with rotating band) and rear part - boat tail (shape of truncated cone). The aerodynamic shape of a projectile is very well known. The precise dimensions and construction of the projectile determine the specific physical effects of air flow. The determination of effects of air flow on the projectile with adequate aerodynamic flow model and the verification of calculated values in relation to the test values are of significance.

The importance of an accurate estimate is obvious because the classic symmetric projectile with muzzle velocity as the main energy resource flies to target, without any other influence but drag or aerodynamic force.
Aerodynamic coefficients and derivatives of projectile model are calculated with adopted models of calculation (aerodynamic prediction) and determined experimentally as function of Mach numbers and angle of attack of projectile model. The comparative analysis of experimental and calculated values of aerodynamic coefficients of projectile model is done.

2. Model of classic axis-symmetrical projectile

Presented model is projectile 40 mm Bofors (projectile type M), figure 1. Stability of this unmanned projectile is described by parameters of stability (angle of attack, amplitude absorber coefficients and factors of dynamic stability and gyroscopic stability). These parameters are calculated on the basis of values of aerodynamic coefficients (determined by semi-empirical calculation - calc. and experimentally - exp. in three-sonic wind tunnel).

The object of the research is the model of the classic symmetric projectile with following characteristics:

- Reference diameter (caliber) : 40 mm,
- Total length : 206,8 mm,
- Nose length : 122,5 mm,
- Boat tail length : 18 mm,
- Center of mass : 151,8 mm,
- Mass: 0,985 kg.

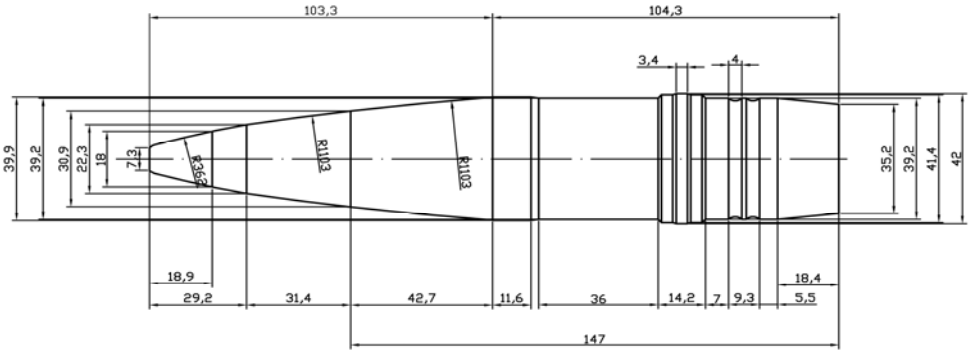

Figure 1. Model of classic axis-symmetrical projectile (type M).

The projectile is assumed to be either a body of revolution whose spin axis coincides with a principal axis of inertia, or a finned missile with three or more identical fins spaced symmetrically around the circumference of a body of revolution. In addition to the requirements of configuration and mass symmetry, the projectile is also restricted to small yaw flight along its trajectory. In conventional aircraft aerodynamics, the terms “pitch” or “angle of attack” refer to the aircraft’s nose pointing above or below its flight path; the terms “yaw” or “angle of sideslip” refer to the nose pointing to the left or right of the flight path, [2]. The aerodynamic drag force opposes the forward velocity of the projectile and that is the classical aerodynamic force of exterior ballistics known as the “air resistance”.

3. Aerodynamic coefficients of classic axis-symmetrical projectile

Aerodynamic forces and moments acting on the model are calculated with two semi-empirical methods (aerodynamic prediction): ADK0 and ADK1, [6]. Calculated values of aerodynamic coefficients are compared with experimental values for all components of force and moment [4].

The aerodynamic force acting on projectile in the centre of pressure is given by, [1]:

$$R = \begin{bmatrix} X \\ \overline{Y} \\ \overline{Z} \end{bmatrix} = q_\infty S \begin{bmatrix} C_x \\ C_{\overline{Y}} \\ C_{\overline{Z}} \end{bmatrix}. \tag{1}$$

and aerodynamic moment acting on projectile,

$$M^R = \begin{bmatrix} L \\ \overline{M} \\ \overline{N} \end{bmatrix} = q_\infty S\, d \begin{bmatrix} C_L \\ C_{\overline{M}} \\ C_{\overline{N}} \end{bmatrix}. \tag{2}$$

$q_\infty = \frac{\rho V_\infty^2}{2}$ - dynamic pressure,

$S = \frac{d^2 \pi}{4}$ - projectile referent area,

d - referent diameter - caliber,

$C_x, C_{\overline{Y}}, C_{\overline{Z}}$ - aerodynamic coefficients of aerodynamic forces,

$C_L, C_{\overline{M}}, C_{\overline{N}}$ - aerodynamic coefficients of aerodynamic moments,

ρ - air density,

$\vec{V}_\infty$ - the vector velocity.

These aerodynamic coefficients representing aerodynamic forces $C_x, C_{\overline{Y}}, C_{\overline{Z}}$ and aerodynamic moments $C_L, C_{\overline{M}}, C_{\overline{N}}$ depend on:

- airflow characteristics (Mach number, Reynolds number),
- aerodynamic velocity,
- the angle of attack - σ,
- the angular velocity vector $\vec{\Omega}$ of the body frame with respect to the $\vec{I}$ frame.

The components of aerodynamic force and moment are:

X - Axial aerodynamic force,

$\overline{Y}$ - Side aerodynamic force,

$\overline{Z}$ - Normal aerodynamic force,

L - Aerodynamic Rolling moment,

$\overline{M}$ - Aerodynamic Pitching moment,

$\overline{N}$ - Aerodynamic Yawing moment.

This paper considers numerical calculation of these aerodynamic coefficients of forces and moments. To calculate any of these coefficients it is necessary to know the influence of aerodynamic parameters and their interaction.

The axial aerodynamic force coefficient is given by equation (3) and depends on Mach number and the angle of attack σ , [1]. That force represents the main component of the total aerodynamic force (Drag),

$$C_X = C_{X0}\left(Ma\right) + C_{X\sigma^2}\left(Ma\right)\cdot\sigma^2 . \tag{3}$$

Aerodynamic axial coefficient $C_{X0}\left(Ma\right)$ depends on Mach number and the shape of the projectile, [1].

The normal force coefficient depends on the angle of attack, Mach number and Reynolds number, given by [1],

$$C_{\overline{Z}} = C_{\overline{Z}\sigma}\left(Ma\right)\sigma + C_{\overline{Z}\sigma^3}\left(Ma\right)\cdot\sigma^3 . \tag{4}$$

The pitching moment coefficient also depends on the angle of attack, Mach number and Reynolds number, [1] described by equation (5). It consists of static derivative which is caused by normal force and dynamic derivative caused by the change of the angle of attack σ and pitching velocity $\overline{q}$.

$$C_{\overline{M}} = C_{\overline{M}\sigma}\sigma + C_{\overline{M}\sigma^3}\sigma^3 + C_{\overline{M}\dot{\sigma}}\dot{\sigma}^* + C_{\overline{M}q}\overline{q}^* . \tag{5}$$

The side aerodynamic force and the yawing aerodynamic moment are also called Magnus effect. They depend on the projectile shape, Mach number, Reynolds number, yawing angular velocity $\overline{r}$ and the angle of attack, [1]. The coefficients of the force and the moment consist of the derivatives. Magnus force coefficient represents the derivative of angle of attack and rolling angular velocity p

$$C_{\overline{Y}}\left(p^*,\sigma\right) = \left(C_{\overline{Y}p\sigma} + C_{\overline{Y}p\sigma^2}\sigma^2\right)p^*\sigma . \tag{6}$$

Magnus moment coefficient represents the act of the side force at the attack point i.e. the derivative of the angle of attack and rolling angular velocity, as

$$C_{\overline{N}}\left(p^*\sigma\right) = \left(C_{\overline{N}p\sigma_0} + C_{\overline{N}p\sigma^2}\sigma^2\right)p^*\sigma . \tag{7}$$

The Magnus force and moment are of lower values than the normal force and the pitching moment, i.e. they point at the stability of flight and the precision of the weapon‘s system.

The rolling aerodynamic moment coefficient depends on the rolling angular velocity p , Mach number, Reynolds number and the angle of attack σ , [1]. The most influential parameter, the rolling angular velocity, defines the derivative of aerodynamic coefficient of rolling moment which is also called the spin dumping moment coefficient and is given by (8).

$$C_L = C_{Lp}p^* . \tag{8}$$

3.1. Aerodynamic prediction

This paper deals with mathematical interpretation of presented aerodynamic coefficients. These mathematical equations are given on the basis of theoretical research presented with partial differential equation and solved by finite elements method [1, 2]. Also, some

derivatives are improved in relation of measurements and results of the experiments. The results of the numerical calculation of the derivatives and aerodynamic coefficients are presented in this chapter.

On the basis of these geometric and dynamic characteristics, according to the calculation by aerodynamic prediction [1, 2, and 7], the aerodynamic coefficients and its derivatives are calculated. Mach number best represents the characteristics of airflow, i.e. the velocity of the projectile in relation to the sonic velocity.

3.2. Experimental results of aerodynamic coefficients

The T-38 wind tunnel facility. The T-38 test facility of Military Technical Institute in Belgrade is a blow down type pressurized wind tunnel with a 1.5m x 1.5m square test section [7]. For subsonic and supersonic tests, the test section is with solid walls, while for transonic tests, a section with porous walls is inserted in the tunnel configuration. The porosity of walls can be varied between 1.5% and 8%, depending on Mach number, so as to achieve the best flow quality.
Mach number in the range 0.2 to 4.0 can be achieved in the test section, with Reynolds numbers up to 110 million per meter. In the subsonic configuration, Mach number is set by sidewall flaps in the tunnel diffuser. In the supersonic configuration, Mach number is set by the flexible nozzle contour, while in transonic configuration, Mach number is both set by sidewall flaps and the flexible nozzle, and actively regulated by blow-off system. Mach number can be set and regulated to within 0.5% of the nominal value.
Stagnation pressure in the test section can be maintained between 1.1 bar and 15 bar, depending on Mach number, and regulated to 0.3 % of nominal value. Run times are in the range 6s to 60s, depending on Mach number and stagnation pressure.
Model is supported in the test section by a tail sting mounted on a pitch-and-roll mechanism by which desired aerodynamic angles can be achieved. The facility supports both step-by-step model movement and continuous movement of model (“sweep”) during measurements.

Range of test. Tests of the model were performed in the Mach number range from 0.2 to 3.0 (14 different values of Mach number). The complex angles of attack were in the interval from –10° to +10° (21 different values of angle of attack) and roll angle was 0°.

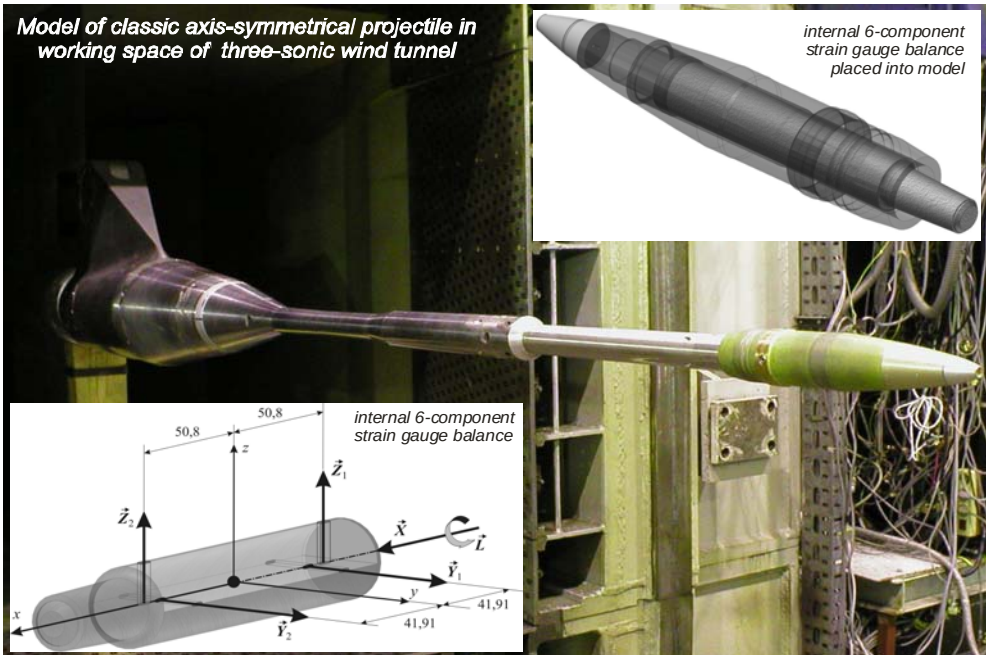

Figure 2. Model of classic axis-symmetrical projectile in wind tunnel.

Aerodynamic forces and moments acting on the model were measured by ABLE 1.00 MKXXIIIA internal six-component strain gauge balance. Nominal load range of the balance was 2800 N for normal, 620 N for side forces, 134 N for axial force, 145 Nm for pitching, 26 Nm for yawing moment and 17 Nm for rolling moment; the accuracy was approximately 0.25% F.S. for each component.

Instrumentation and data recording. Data reduction was performed after each run, using the standard T38-APS software package in use with the wind-tunnel facility. It was done in several stages, i.e.:

- Data acquisition system interfacing and signals normalization;
- Determination of flow parameters in the test section of the wind tunnel;
- Determination of model position (orientation) relative to test section and airflow;
- Determination of non-dimensional aerodynamic coefficients of forces and moments.

Each stage has been performed by a different software module.

The stagnation pressure P_0 in the test section was measured by a *Mensor* quartz bourdon tube absolute pressure transducer pneumatically connected to a Pitot probe in the settling chamber of the wind tunnel. Range of the transducer used was 7 bar.

The difference (P_{st} -P_0) between the stagnation and static pressure in the test section was measured in subsonic/transonic speed range by a *Mensor* quartz bourdon tube differential pressure transducer, pneumatically connected to the P_0 Pitot probe and to an orifice on the test section sidewall. In transonic and supersonic speed ranges an absolute pressure transducer of same type and range was used. Range of these transducers was 1.75 bar;

Atmospheric pressure P_{atm} was measured by a *Mensor* quartz bourdon tube absolute pressure transducer pneumatically connected to a pressure port in the wind tunnel exhaust. Range of these transducers was 1.75 bar.

The stagnation temperature T_0 was measured by a custom-made RTD probe in the settling chamber of the wind tunnel.

The pitching and rolling angle of the model support measured by *NPL* resolvers integrated in the model support mechanism. The accuracy of the pitching angle reading was 0.05° and of the rolling angle reading was 0.25°.

Aerodynamic forces and moments acting on the model were measured by ABLE 1.00 MKXXIIIA internal six-component strain gauge balance. Nominal load range of the balance was 2800 N for normal, 620 N for side forces, 134 N for axial force, 145 Nm for pitching, 26 Nm for yawing moment and 17 Nm for rolling moment; the accuracy was approximately 0.25% F.S. for each component.

The data acquisition system consisted of a *Teledyne* 64 channels "front end" controlled by a *PC* computer. The front-end channels for flow parameters transducers (i.e. transducers for P_0, P_{st} -P_0 and T_0) were set with 30 Hz, fourth-order low pass Butterworth filters and appropriate amplification. The data from all analog channels were digitized by a 16-bit resolution A/D converter with the overall accuracy of the acquisition system being about 0.05% to 0.1% F.S. of the channel signal range. All channels were sampled with the same 200 samples/s rate.

3.3. Comparison of calculated values and test results

Calculated values of aerodynamic coefficients are compared with experimental values for all components of force and moment. The most important components of aerodynamic coefficients of axis-symmetrical projectile: axial force for zero angle of attack and pitching moment are presented in Fig. 3.

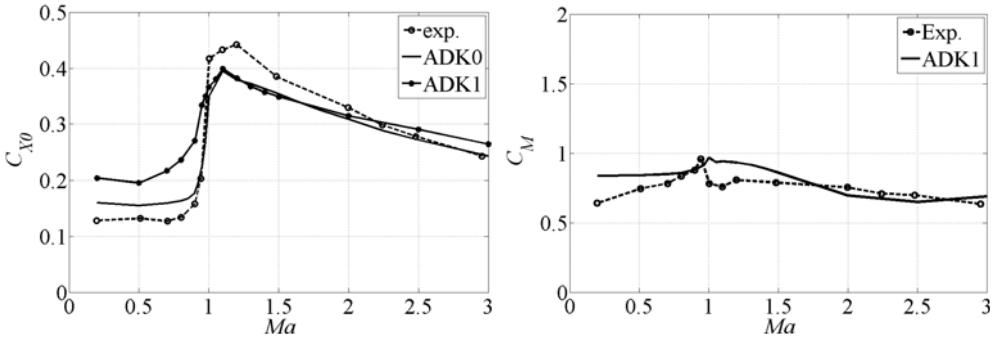

a) axial force b) pitching moment

Figure 4. Calculated and experimental values of aerodynamic coefficient.

The characteristic function of aerodynamic coefficients in relation to angle of attack is presented in the following figure 4.

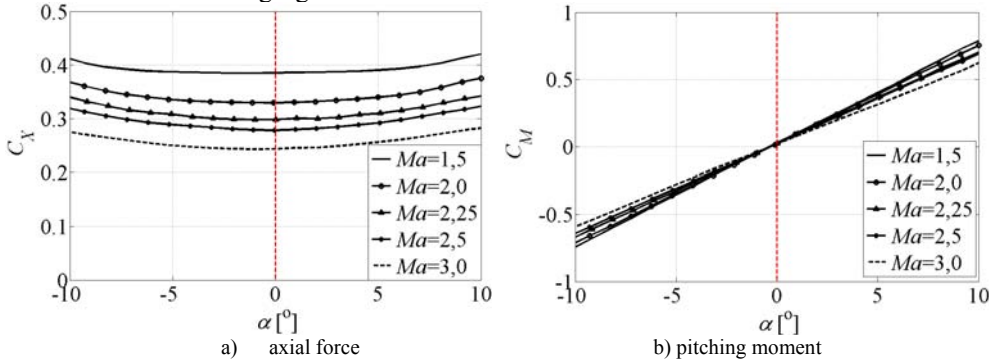

a) axial force b) pitching moment

Figure 4. Aerodynamic coefficient for different values of angle of attack.

4. Model of flight stability

The evaluation of projectile dynamic stability is defined by Lapunov criterion. Quantitative disturbances are: maximum amplitude of disturbed value in regard to nominal value, period of transitional process (dumping), periodic or aperiodic behavior. The aim of the research is to achieve dynamic stability of projectile, i.e. to make the maximal amplitude of disturbed value to converge to nominal value, such as the angle of attack.
The general solution of complex inhomogeneous differential equation is sum of solution of homogeneous differential equation and one particular solution of inhomogeneous differential equation $\widetilde{\boldsymbol{\xi}} = \widetilde{\boldsymbol{\xi}}_h + \widetilde{\boldsymbol{\xi}}_p$. The homogeneous solution is caused by initial trajectory disturbances and particular solution is caused by acceleration of gravitation and aerodynamic asymmetry. The coefficients of homogeneous part of complex differential equation do not depend upon flight velocity. The variables depend on the change of aerodynamic coefficient with the change of Mach number.
The prediction of stability of axis-symmetrical projectile is determined by observing the value variations of damping coefficients $\boldsymbol{\lambda}_1$ and $\boldsymbol{\lambda}_2$, and evaluating the relationship factors of dynamic S_g and gyroscopic S_d flight stability.

4.1. Gyroscopic and dynamic stability of symmetrical projectile

Frequency equation

$$\Phi_j = \frac{1}{2}\left[P \pm \sqrt{P^2 - 4M}\right], \quad j = 1,2 \tag{1}$$

depend on Murphy's coefficients P and M :

$$P = \frac{I_x}{I_y} \cdot \frac{p \cdot d}{V}$$

$$M = \frac{C^*_{\bar{m}\boldsymbol{\sigma}} - C^*_{\bar{m}\dot{\boldsymbol{\sigma}}} \cdot \dfrac{V'}{V} - C^*_{\bar{m}q} \cdot C^*_{\bar{z}\boldsymbol{\sigma}}}{\bar{r}_y^2}$$

where:

$$C^*_{\bar{m}\boldsymbol{\sigma}} = E \cdot C_{\bar{m}\boldsymbol{\sigma}}$$

$$C^*_{\bar{m}\dot{\boldsymbol{\sigma}}} = E \cdot C_{\bar{m}\dot{\boldsymbol{\sigma}}}$$

$$C^*_{\bar{m}q} = E \cdot C_{\bar{m}q}$$

$$C^*_{\bar{z}\boldsymbol{\sigma}} = E \cdot C_{\bar{z}\boldsymbol{\sigma}}$$

$$C^*_x = E \cdot C_x$$

$$E = \frac{\boldsymbol{\rho} \cdot S \cdot d}{m}$$

$$V' = C^*_x$$

The criterion of gyroscopic stability for full linearized solution is:

$$\left(P^2 - 4M\right) > 0 \tag{2}$$

According to classic exterior ballistics, gyroscopic stability factor is defined by:

$$S_g = \frac{P^2}{4M} \tag{3}$$

By eliminating P^2 in equations (2) and (3):

$$4M\left(S_g - 1\right) > 0 \tag{4}$$

In case of gyroscopic stabilized projectile, where Murphy's coefficient is $M > 0$, equation (3) is simplified and criterion of gyroscopic stability is given by:

$$S_g > 1 \text{ or } \frac{1}{S_g} < 1.$$

The main condition for dynamic stability is that both damping coefficients are less than zero ($\lambda_1 < 0$ and $\lambda_2 < 0$) during all flight period. During the real flight, it is possible that damping coefficient becomes positive, for a short time period, and then reestablishes negative values, without significant influence on flight. If the positive trend of damping coefficients remains during the flight, the projectile becomes instable on the trajectory.

Static stable projectile without spin (or with small axial rotation) has values of Murphy's coefficient $M < 0$, and spin velocity p is equal to zero or small enough that might be neglected.

Dumping coefficients equation, represented by:

$$\lambda_j = -\frac{1}{2}\left[H \mp \frac{P(2T - H)}{\sqrt{P^2 - 4M}}\right], \quad j = 1,2 \tag{5}$$

shows that, in this particular case, only condition for dynamic stability is that Murphy's coefficient $H > 0$. In case of wing stabilized projectile, the sum of dynamic derivative of aerodynamic coefficients is usually negative, $\left(C_{mq} + C_{m\dot{\sigma}}\right) < 0$.

The aerodynamic coefficient of normal force is usually negative, $C_{z\sigma} < 0$. In this way, the dynamic stability is provided, because the Murphy's coefficient is positive, i.e. $H > 0$.

$$H = -C^*_{z\sigma} - \frac{\left(C^*_{mq} + C^*_{m\dot{\sigma}}\right)}{\bar{r}_y^2} \tag{6}$$

Where

$$C^*_{\bar{z}\sigma} = E \cdot C_{\bar{z}\sigma}$$

$$C^*_{mq} = E \cdot C_{mq}$$

$$C^*_{m\dot{\sigma}} = E \cdot C_{m\dot{\sigma}}$$

$$E = \frac{\rho \cdot S \cdot d}{2m}$$

Regarding to the equation (5), it is concluded that dumping coefficients λ_j will be negative, respectively to the following condition

$$\left[H \mp \frac{P(2T - H)}{\sqrt{P^2 - 4M}}\right] > 0 \tag{7}$$

The dynamic factor of stability S_d is defined by Murphy's coefficients

$$S_d = \frac{2T}{H} \tag{8}$$

The insertion of equation (8) in equation (7) leads to following inequalities, where both inequalities have to be fulfilled to achieve dynamic stability,

$$H > 0 \tag{9}$$

$$\left[\frac{P^2(S_d-1)^2}{P^2-4M}\right] < 1 \tag{10}$$

The solution of inequality (10) gives

$$P^2(S_d-1)^2 < P^2 - 4M$$

$$(S_d-1)^2 < 1 - \frac{4M}{P^2}$$

$$S_d{}^2 - 2S_d + 1 < 1 - \frac{4M}{P^2}$$

$$S_d(2-S_d) > \frac{4M}{P^2} \tag{11}$$

The insertion of equation (3) in inequality (11) gives following inequality:

$$\frac{1}{S_g} < S_d(2-S_d) \tag{12}$$

Equations (9) and (12) describe general criteria of dynamic stability for any axis-symmetrical projectile with or without wing stabilizer. Most types of projectiles can be classified in two groups: static stable type of projectiles without axial rotation or slow-spin projectiles and static instable type of projectiles which have to be gyroscopically stabilized.

5. Analysis of parameters of stability

Motion of projectile is simulated through six-degrees of freedom model (6-DOF). Comparative analysis of calculated and experimental parameters of stability is presented in figures as dependencies of angles of attack, dumping coefficients and factors of dynamic and gyroscopic stability on time and path.

Preliminary qualitative evaluation of projectile flight stability is determined through analysis of components of total angle of attack. At initial part of trajectory, disturbances cause deviation of velocity vector from longitudinal axis of projectile. Values of angle of attack α and side-slip angle β should decrease during the flight. This would provide initial qualitative condition of stable flight. The angle of attack α and side-slip angle β versus time flight and distance in initial part of trajectory is presented in the Fig. 5. Results of flight simulation are presented in regard to two different groups of initial data: experimental values (*exp*) and calculated prediction (*calc*) of aerodynamic coefficients for model of axis-symmetrical projectile.

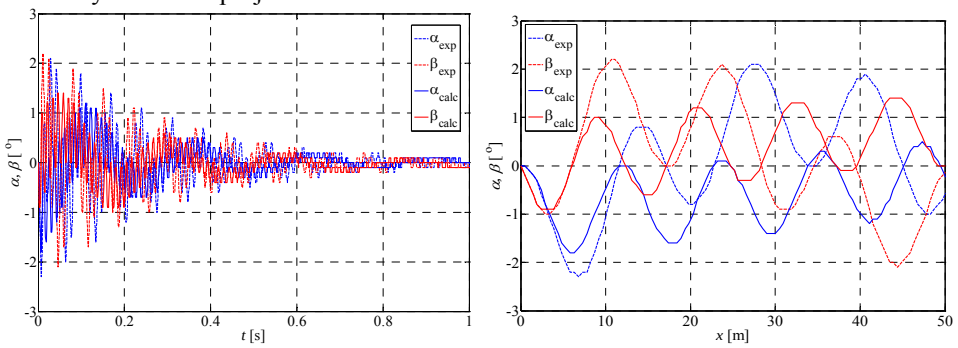

a) vs. time b) vs. distance

Figure 5. Components of angle of attack in initial part of trajectory.

The analysis of flight stability is performed according to six-degrees of freedom simulation using experimental and calculated values of aerodynamic coefficients for same flight conditions. Qualitative stability analysis is performed with regard to stability equations and inequalities of dumping coefficients and stability factors. Stability parameters determined by 6-DOF flight simulation of model of projectile are presented in figure 6. Trajectory simulation is performed according to experimental (exp) and calculated (calc) values of aerodynamic coefficients. In the figure 5 a) preliminary conditions of stable flight as negative values of dumping coefficients during the flight ($\lambda_j < 0$) are presented. In the figure 5 b) final and sufficient condition of stable flight, as relation of gyroscopic and dynamic factors of stability, is presented and given by inequality (E12).

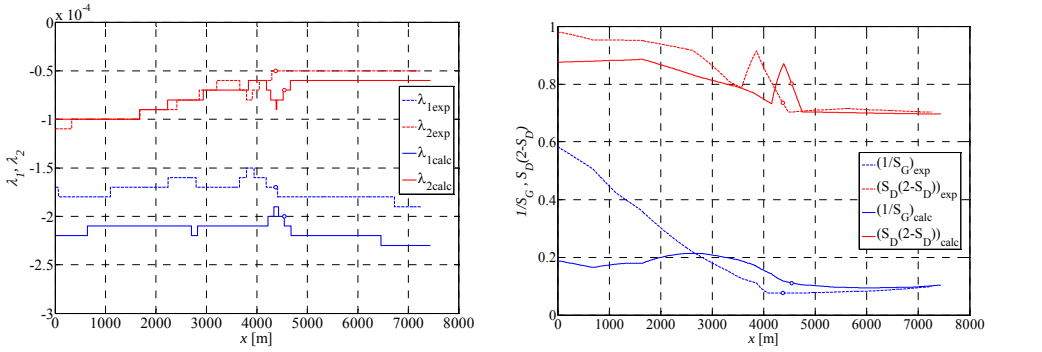

a) dumping coefficients b) dynamic and gyroscopic factors of stability

Figure 6. Stability parameters.

Presented results of stability research for model of axis-symmetrical projectile, Fig. 1, describe a type of static instable projectile stabilized with longitudinal rotation.

5. Effects of aerodynamic coefficients on projectile stability

The investigation of stability properties is performed according to stability equations using 6-DOF flight simulation. The stability of flight depends of aerodynamic properties, represented by components of aerodynamic force and aerodynamic moment. Relative differences between calculated and experimental values of aerodynamic coefficients are 5 % to 15 %, depending on flow regime. Therefore, the determination of effects of aerodynamic coefficients on stability parameters is performed for value range of all aerodynamic coefficients and their derivatives.
Values of aerodynamic coefficients and derivatives are changed from -15 % up to +15 %. According to this value range as input parameters of 6-DOF flight simulation, the values of parameters of stability of projectile and their characteristics are analyzed.

Aerodynamic coefficient of axial force C_{X0} has the most significant impact on trajectory characteristics and stability parameters. The increase of values of axial aerodynamic coefficient of 5 to 15% shows the boost of most of stability parameters and the decrease of the spin velocity of 3 down to 8%. Dumping coefficient λ_2 and gyroscopic stability expression $(1/Sg)$ are increased up to 20%, and dynamic stability expression $(Sd(2-Sd))$ is increased up to 5%. In case of decrease of axial coefficient, above mentioned parameters are decreased in the same manner.
The derivative of aerodynamic coefficient of normal force $C_{Z\sigma}$ influences mostly on dumping coefficient λ_2 and on dynamic stability expression $(Sd(2-Sd))$. The decrease of the normal force derivative of 5 to 15% shows decreasing dumping coefficient λ_2 down to 20%, and decreasing

dynamic stability expression $\left(Sd\left(2-Sd\right)\right)$ down to 6%. The increasing of normal force derivative up to 15 % leads to increase in the similar manner: dumping coefficient λ_2 up to 20% and dynamic stability expression $\left(Sd\left(2-Sd\right)\right)$ up to 5%.

The influence of aerodynamic coefficient of pitching moment is analyzed through separate analyses of static derivative $C_{M\sigma}$ and dynamic derivatives of pitching moment (dynamic derivatives of stability) $C_{M\dot{\sigma}}+C_{Mq}$. The increase of static pitching derivative shows proportional rise of gyroscopic stability expression $\left(1/Sg\right)$ up to 15% and the decrease of static derivative leads to proportional depletion of gyroscopic stability down to 15%.
Dynamic derivatives of pitching moment $C_{M\dot{\sigma}}+C_{Mq}$ show larger influence on stability parameters, especially on dumping coefficient λ_1, which values are decreased down to 30% in regard to increasing of dynamic derivatives up to 15%. Also, dynamic stability expression $\left(Sd\left(2-Sd\right)\right)$ is decreased 2.5 % down to 7%. The depletion of dynamic derivatives causes the rise of dumping coefficient λ_1 up to 30% and dynamic stability expression up to 8%.

The rise of derivative of aerodynamic coefficient of rolling moment of 15% causes the increase of gyroscopic stability factor expression $\left(1/Sg\right)$ up to 25% and the decreasing spin velocity down to 12%. The decrease of derivative of aerodynamic coefficient of rolling moment causes the decrease of gyroscopic stability factor expression $\left(1/Sg\right)$ down to 25% and the increasing spin velocity up to 14%.

The effects of derivatives of aerodynamic coefficient of side force and yawing moment (Magnus force and moment) show the decrease of stability parameters. The rise and decrease of these derivatives of 5 to 15% cause only the rise of stability parameters. The derivative of aerodynamic coefficient of side force $C_{Yp\sigma}$ causes the increase of dumping coefficients λ_1,λ_2 of 20% and dynamic stability factor expression of only 2%. The derivative of aerodynamic coefficient of yawing moment $C_{Np\sigma}$ causes the rise of dumping coefficients λ_1,λ_2 of 30% and dynamic stability factor expression of 25%.
These three coefficients, axial force, normal force and pitching moment are the most influential forces and moments on the projectile flight. Using the experimental results, as in theory, side force and yawing moment are less significant for flight trajectory.

6. Conclusion

The stability of classic axis-symmetrical projectile is affected by aerodynamic coefficients through a steady influence of the axial aerodynamic coefficient on most of the stability parameters and through the strongest influence of dynamic derivative of aerodynamic coefficient of pitching moment and derivative of aerodynamic coefficient of yawing moment on dumping coefficients and factor of dynamic stability.

During the test the real model was used and the measures obtained are not transformed, thus the results are correct.
The trait of the change of the calculated values of aerodynamic coefficients coincides with the experimental results of aerodynamic coefficients.
The values of axial aerodynamic force coefficient are higher than the calculated values and particularly in the transonic field. The increase of the values in transonic field is due to the influence of the

supporter which diameter is similar to the projectile base diameter. However, in subsonic field the values of experimental axial aerodynamic force coefficient are lower than calculated values of that coefficient. This is due to the projectile base which is covered with the supporter and there is no whirlpool. The aerodynamic resistance caused by the whirlpool behind the projectile in subsonic field is the main part of the total aerodynamic resistance.
In transonic field the main part of the aerodynamic resistance is in the sound wave resistance.

The experimental results confirmed the correctness of the numerical calculation to a great extent. The accurate numerical calculation enables the exact determination of the aerodynamic characteristics. The exact aerodynamic coefficients show the real acting of forces and moments on the projectile during the flight. The values of the obtained coefficients are easily used in the equations that describe a model of the projectile flight – model 6 degrees of freedom and model of modified point mass.

Acknowledgement
The authors would like to thank the management and staff of the Wind tunnel T38 of Military Technical Institute for hosting the experiment.

References

[1] Regodić, D., *Spoljna balistika*, Vojna akademija, Beograd, 2006., pp. X11-X12
[2] Lebedev A.A., Cernobrovkin L.S., *Dinamika poleta*, Mashinostroenie, Moskva, 1973.
[3] Ristic S., *Flow visualization technics in wind tunnel*, VTI, Belgrade, 1996.
[4] Samardzic M., *Testing of Projectile model of 40 mm in T-38 wind tunnel, V3- 2982 VTI Beograd, 2008.*
[5] Elfstrom G.M., Medved B.; *The Yugoslav 1.5m Trisonic Blowdown Wind Tunnel,* AIAA Paper 86-0746-CP
[6] Jerkovic D., Samardzic M., *The aerodynamic characteristics determination of classic symmetric projectile*, The 5th international symposium about design in mechanical engineering KOD 2008, ISBN 978-86-7892-104-9, pp. 275-282, Novi Sad, 2008.

NUMERICAL SIMULATION OF PERTURBED POISEUILLE-COUETTE FLOW

M. Jovanović, J. Nikodijević

[1] Chair for Hydroenergetics, Faculty of Mechanical Engineering
University of Nis, A.Medvedeva 14, 18000 Nis, Serbia
e-mail: jmilos@masfak.ni.ac.rs
[2] Faculty of Mechanical Engineering
University of Nis, A.Medvedeva 14, 18000 Nis, Serbia,
e-mail: coldfluids@gmail.com

Abstract. The flow between two coaxial rotating cylinders can be represened as Couette fluid flow if the ration between the radius $(R_2-R_1)/R_2 \ll 1$. In this paper the case of the flow with streamwise favorable (dp/dx>0) has been considered. The flowfield has been simulated in direct numerical fashion, without any averages not in spatial and nor in temporal sense. We have used our numerical code for full 2D Navier-Stokes equations using Fourier series in homogeneous direction, and Chebyshev polynomials in nonhomogeneous direction. For time discretiztion discretization we have used Adams-Bashwort semi implicit two-step method. We have solved momentum equation in vorticity-streamfunction form, and since we had two boundary conditions for streamfunction and none for vorticity, we resolved this problem by using influence matrix method. The evolution of flow field for velocity has been shown for the intial nondimensional time period $0 \leq t \leq 9\pi$.

.

1. Introduction

In this paper we consider two-dimensional direct numerical simulation of Navier-Stokes equations in vorticity-streamfunction formulation. We have chosen the Couette-Poiseuille flow configuration which is equivalent to fluid flow between two coxial cylinder in circumferential direction when the ratio $(R_2-R_1)/R_2 \ll 1$, where R_2 is outer and R_1 is inner radius of cylinder. The inner cylinder rotates in counter-clockwise direction and outer cylinder rotates in clockwise direction where it is valid $\omega_1 R_1 = \omega_2 R_2$. The exact solution for Couette- Poiseuille flow is perturbed by optimized linear combination of eigenvectors obtained as solution of Orr-Sommerfeld perturbation eqation for the case of Couette-Poiseuille flow.

2. Combined plane Couette and plane Poiseuille flow

The Couette-Poiseuille flow is described as a flow between two parallel plates, where the plates move in oposite direction with the same velocity (Couette flow) and where the constant pressure gradient is imposed in streamwise direction (Poiseuille flow). This flow can be described in the following manner:

$$U(y) = A\left(1 - y^2\right) + By, \quad (-1 \le y \le 1), \tag{1}$$

Where $0 \le A \le 1$ and $0 \le B \le 1$. The choice of a characteristic velocity is still at our disposal. If we require that max U(y)=1, then A and B must be related by

$$B = \begin{cases} 1 & (0 \le A \le 1/2) \\ 2\left[A(1-A)\right]^{1/2} & (1/2 \le A \le 1), \end{cases} \tag{2}$$

And we thus have a one-parameter family of velocity profiles. For A=0 and B=1 we have Couette flow,and for A=1 and B=0 we obtain plane Poiseuille flow. In the case $A \neq 0$ and $B \neq 0$ we get combined plane Couette-Poiseuille flow.

In the prevous papers [1] and [2] we have used pseudo specral method [3] to describe vorticity evolution in 2D channel flow. In this paper we have numerically solved pertubation equation in the way similar to those that is described in literature [5] [6] and [7]..

.

3. Finite amplitude stability problem-nonlinear stability

For linear stability analysis we concern to find critical values for infinitesimal peruturbation to veloctiy profile, but in the case of nonliear stability our mayor task is to find how the finite amplitude disturbances influence the fluid flow stability trought the viscous fluid flow evolution, which can be carried out by full Navier-Stokes equation numerical simulation, see [8] and [9].

The theoretical investigations are based on the assumption that laminar flows are affected by small disturbances; for channel flow, these disturbances originate at the inlet whereas for the boundary layer over a flat plate placed in a stream they are due to roughness on the solid surface or irregularities in the external flow. The stability theory is to follow up in time the behavior of such disturbances, then they are imposed on the main flow and whether the disturbances increase or die out with time.

If the disturbances decay with time, the main flow is considered stable; in contrast, if the disturbances amplify with time the main flow is unstable and the possibility of transition to turbulence exists. Stability theory predicts the value of the critical Reynolds number, beyond which instability will exist for a prescribed main flow. For plane incompressible viscous Couette flow, the flow is unconditionally stable at all Reynolds numbers. The viscosity is known to have a stabilizing effect on the flow. In case of the plane Poiseuille flow, the flow is stable at low Reynolds numbers Re<5772.

The mathematical problem is the determination of the eigenvalues of the stability equation obtained from the governing conservation equations of mass and momentum. It is the aim of the stability analysis to compute the phase velocity, rate of amplification and the wave number of all possible disturbances, in a given flow as a function of the relevant flow properties such as Reynolds number.

In our case of plane Couette–Poiseuille flow the 2D Navier Stokes equations are

$$\begin{aligned}
&\frac{\partial u}{\partial t}+u\frac{\partial u}{\partial x}+v\frac{\partial u}{\partial y}=\frac{1}{\rho}\frac{\partial p}{\partial x}+\nu\left(\frac{\partial^2 u}{\partial x^2}+\frac{\partial^2 u}{\partial y^2}\right),\\
&\frac{\partial v}{\partial t}+u\frac{\partial v}{\partial x}+v\frac{\partial v}{\partial y}=\frac{1}{\rho}\frac{\partial p}{\partial y}+\nu\left(\frac{\partial^2 v}{\partial x^2}+\frac{\partial^2 v}{\partial y^2}\right),\\
&\frac{\partial u}{\partial x}+\frac{\partial v}{\partial y}=0,\left(-1\le y\le 1\right),\left(0\le x\le 2\pi\right).
\end{aligned} \tag{3}$$

u-streamwise velocity, *v*-normal velocity, p-pressure and *ν*-kinematic viscosity. To study its stability we put

$$\begin{aligned}
&\vec{u}\left(\vec{r},t\right)=U\left(y\right)\vec{i}+u'\left(\vec{r},t\right),\\
&\vec{v}\left(\vec{r},t\right)=v'\left(\vec{r},t\right),\\
&p\left(\vec{r},t\right)=P_0+p'\left(\vec{r},t\right).
\end{aligned} \tag{4}$$

and substitute this expressions into equations (3), and neglect quadratic terms in the small primed quantities to derive the linearized equations for the disturbance. We take normal modes of the form

$$\begin{aligned}
&u'\left(\vec{r},t\right)=\hat{u}\left(y\right)e^{i\alpha\left(x-ct\right)}\\
&v'\left(\vec{r},t\right)=\hat{v}\left(y\right)e^{i\alpha\left(x-ct\right)}\\
&p'\left(\vec{r},t\right)=\hat{p}\left(y\right)e^{i\alpha\left(x-ct\right)}
\end{aligned} \tag{5}$$

and supstitute them in the equations (3). Here α-stream-wise wavenumber and *c*-phase velocity of perturbation, whereas $\hat{u}\left(y\right)$ $\hat{v}\left(y\right)$ and $\hat{w}\left(y\right)$ are comlex numbers. Thus the first equation in (3) when nonlinear terms are neglected gives

$$\begin{aligned}
&i\alpha\left[U\left(y\right)-c\right]\hat{u}\left(y\right)=\\
&=-\frac{i\alpha}{\rho}\hat{p}\left(y\right)+\nu\left(i^2\alpha^2\hat{u}\left(y\right)+\frac{\partial^2\hat{u}\left(y\right)}{\partial y^2}\right),
\end{aligned} \tag{6}$$

And the second one is

$$\begin{aligned}
&i\alpha\left[U\left(y\right)-c\right]\hat{v}\left(y\right)=\\
&=-\frac{1}{\rho}\frac{\partial\,\hat{p}\left(y\right)}{\partial\, y}+\nu\left(i^2\alpha^2\hat{v}\left(y\right)+\frac{\partial^2\hat{v}\left(y\right)}{\partial y^2}\right),
\end{aligned} \tag{7}$$

The conitnuity equations is

$$i\alpha\hat{u}\left(y\right)+\frac{\partial\,\hat{v}\left(y\right)}{\partial\, y}=0, \tag{8}$$

One may eliminate $\hat{p}(y)$ from (6) and (7) if we differentiate (6) with regard to y and multiply (7) with $i\alpha$, and than substract from each other. In that case we have

$$\begin{aligned} &-i\alpha c\frac{\partial \hat{u}(y)}{\partial y}+i\alpha\left[\frac{\partial U(y)}{\partial y}\hat{u}(y)+U(y)\frac{\partial \hat{u}(y)}{\partial y}\right]= \\ &=-\frac{i\alpha}{\rho}\frac{\partial\,\hat{p}(y)}{\partial\, y}+\nu\left(i^2\alpha^2\frac{\partial \hat{u}(y)}{\partial y}+\frac{\partial^3\hat{u}(y)}{\partial y^3}\right), \end{aligned} \tag{9}$$

And and also

$$\begin{aligned} &-(i\alpha)^2 c\hat{v}(y)+(i\alpha)^2 U(y)\hat{v}(y)= \\ &=-\frac{i\alpha}{\rho}\frac{\partial\,\hat{p}(y)}{\partial\, y}+\nu i\alpha\left((i\alpha)^2\hat{v}(y)+\frac{\partial^2\hat{v}(y)}{\partial y^2}\right), \end{aligned} \tag{10}$$

If we now substitute the second equation in the first one, then we get

$$\begin{aligned} &-i\alpha c\frac{\partial \hat{u}(y)}{\partial y}+i\alpha\left[\frac{\partial U(y)}{\partial y}\hat{u}(y)+U(y)\frac{\partial \hat{u}(y)}{\partial y}\right]= \\ &=-(i\alpha)^2 c\hat{v}(y)+(i\alpha)^2 U(y)\hat{v}(y)- \\ &-\nu i\alpha\left((i\alpha)^2\hat{v}(y)+\frac{\partial^2\hat{v}(y)}{\partial y^2}\right)+ \\ &+\nu\left(i^2\alpha^2\frac{\partial \hat{u}(y)}{\partial y}+\frac{\partial^3\hat{u}(y)}{\partial y^3}\right), \end{aligned} \tag{11}$$

Which together with equation (8) and the following boundary conditions

$$\frac{\partial \hat{v}(1)}{\partial y}=0;\quad \hat{v}(1)=0;\quad \frac{\partial \hat{v}(-1)}{\partial y}=0;\quad \hat{v}(-1)=0. \tag{12}$$

form the system of differential equatins to be solved. The equation (12) is fourth order differential equation in $\hat{v}(y)$, which we get after substitution of the continuty equation (8) in it. The described equation is solved by Chebyshev collocation method, and the results of this numerical solution are substituted in (4). So obtained results are incorporated in our numerical code for force term in two dimensional Navier Stokes equation in vorticity-stream function formulation, and the simulation has been carried out in sense of nonlinear stability analysis.

4. Numerical method

Direct numerical simualtion has been carried out for Reynolds number Re=1000, for number of modes N=64 and streamwise wavenumber $\alpha=1.5$ optimized to the phase velocity c=0.9362 and for time step $\Delta t=\pi/200$. Adams-Bashfort semi-implicit time discretization has been used for advancement in time. Time step is suficient small that the phase error and dispersion error are in acceptable limits, in our case ph_error=5.806 10^{-4}.

Navier-Stokes equations for incompressible isothermal flow in vorticity-stream function formulation for two-dimensional flow in nondimensional form read

$$\frac{\partial \omega}{\partial t}+\frac{\partial \psi}{\partial y}\frac{\partial \omega}{\partial x}-\frac{\partial \psi}{\partial x}\frac{\partial \omega}{\partial y}=\frac{\partial f_y}{\partial x}-\frac{\partial f_x}{\partial y}+\nu\left(\frac{\partial^2 \omega}{\partial x^2}+\frac{\partial^2 \omega}{\partial y^2}\right) \tag{13}$$

$$\omega+\frac{\partial^2 \psi}{\partial x^2}+\frac{\partial^2 \psi}{\partial y^2}=0, \tag{14}$$

$$\psi(x,1,t)=g_+(x,t),\ \frac{\partial \psi}{\partial y}(x,1,t)=h_+(x,t)\ , \tag{15}$$

$$\psi(x,-1,t)=g_-(x,t),\frac{\partial \psi}{\partial y}(x,-1,t)=h_-(x,t) \tag{16}$$

$$\psi(x,y,0)=\psi_0(x,y)\ \ on\ \ \Omega. \tag{18}$$

Here ω - is dimensionless vorticity of fluid, ψ -dimension-less stream function, ν-dimensionless kinematic viscosity, f_x and f_y are component of dimensionless body force in co-ordinate x and y axes directions respectively.

The domain Ω is defined as $\Omega=\{(x,y)\in\mathbb{R}^2 \mid 0\le x\le 2\pi \wedge -1<y<1\}$. We have designated the upper domain boundary $\Gamma_u=\{(x,y)\in\mathbb{R}^2 \mid 0\le x\le 2\pi \wedge y=1\}$ and the lower domain boundary $\Gamma_l=\{(x,y)\in\mathbb{R}^2 \mid 0\le x\le 2\pi \wedge y=-1\}$. The time domain is defined as $T=\{t\in\mathbb{R} \mid 0\le t\le T_e\}$, where T_e is the end of the simulation. We have anticipated the periodic boundary conditions in streamwise direction (x-axe), which are in accordance with the periodic perturbations obtained by the solution of (12),(8) and (13) the perturbation equation of hydrodynamic stability.

For the problem stated in the previous section, for the basis functions in x-direction we have taken trigonometric polynomials, and for y-direction we have taken Chebyshev polynomials. The domain in x-direction is equally descretized $\Delta x = 2\pi/N$, and domain in y-direction is descretized by Gauss-Lobatto-Chebyshev points defined as $y_j = \cos(\pi j/N)$ for $0\le j\le N$, where is N-number of discretization points in x- and y-direction. For streamwise direction we have used Fourier-Galerkin method, and for stream normal direction Chebyshev-collocation method. The truncated Fourier series for streamfunction and vorticity read

$$\omega_N(x,y,t) = \sum_{k=-N/2}^{k=N/2} \hat{\omega}_k(y,t)\ e^{Ikx}, \tag{17}$$

$$\psi_N(x,y,t) = \sum_{k=-N/2}^{k=N/2} \hat{\psi}_k(y,t)\ e^{Ikx}. \tag{18}$$

In the above expressions $I=\sqrt{-1}$ is imaginary unit, *k*-wave number, $\hat{\omega}_k(y_j,t)$ and $\hat{\psi}_k(y_j,t)$ are Fourier coefficients for vorticity and streamfunction respectively.. In order to have 2π-periodicity in the flow domain, we have chosen that wave number must be from the set of integers, $k\in\mathbb{Z}$. We apply Fourier-Galerkin method in *x*-direction and then Chebyshev collocation method in *y*-direction to the system of equation (1) and (2), with boundary (3) and (4) and initial conditions (5).

We have introduced the following expression for the curl of body force

$$\mathcal{F} = \frac{\partial f_y}{\partial x} - \frac{\partial f_x}{\partial y} = \sum_{k=-N/2}^{N/2} \hat{\mathcal{F}}_k(x,y,t) e^{Ikx}, \tag{19}$$

and we approximate nonlinear convective terms on left hand side, in the following manner

$$\left(\frac{\partial\psi}{\partial y}\frac{\partial\omega}{\partial x}\right)_N(x,y,t) = \sum_{k=-N/2}^{N/2}\left[\widehat{\frac{\partial\psi}{\partial y}\frac{\partial\omega}{\partial x}}\right]_k(y,t)\, e^{Ikx}, \tag{20}$$

$$\left(\frac{\partial\psi}{\partial x}\frac{\partial\omega}{\partial y}\right)_N(x,y,t) = \sum_{k=-N/2}^{N/2}\left[\widehat{\frac{\partial\psi}{\partial x}\frac{\partial\omega}{\partial y}}\right]_k(y,t)\ e^{Ikx}. \tag{21}$$

Substituting (18),(19),(20),(21) and (22) in (14) and (15) we obtain the following residuals equations

$$\begin{aligned}
&\frac{\partial}{\partial t}\sum_{k=-N/2}^{N/2}\hat{\omega}_k(y,t)e^{Ikx} + \sum_{k=-N/2}^{N/2}\left[\widehat{\frac{\partial\psi}{\partial y}\frac{\partial\omega}{\partial x}}\right]_k(y,t)e^{Ikx} \\
&- \sum_{k=-N/2}^{N/2}\left[\widehat{\frac{\partial\psi}{\partial x}\frac{\partial\omega}{\partial y}}\right]_k(y,t)e^{Ikx} - \sum_{k=-N/2}^{N/2}\hat{\mathcal{F}}_k(y,t)e^{Ikx} \\
&-\nu\left(\frac{\partial^2}{\partial x^2}+\frac{\partial^2}{\partial y^2}\right)\sum_{k=-N/2}^{N/2}\hat{\omega}_k(y,t)e^{Ikx} \neq 0,
\end{aligned} \tag{22}$$

And for definition of vorticity

$$\begin{aligned}
&\sum_{k=-N/2}^{N/2}\hat{\omega}_k(y,t)e^{Ikx} + \\
&+\left(\frac{\partial^2}{\partial x^2}+\frac{\partial^2}{\partial y^2}\right)\sum_{k=-N/2}^{N/2}\hat{\psi}_k(y,t)e^{Ikx} \neq 0.
\end{aligned} \tag{23}$$

If we apply Galerkin method to the equations (23) and (24), i.e. we take for the weight functions the same as basis functions , we obtain

$$\frac{\partial \hat{\omega}_k(y,t)}{\partial t}+\left[\widehat{\frac{\partial \psi}{\partial y}\frac{\partial \omega}{\partial x}}\right]_k(y,t)-\left[\widehat{\frac{\partial \psi}{\partial x}\frac{\partial \omega}{\partial y}}\right]_k(y,t)=$$

$$=\hat{\mathcal{F}}_k(y,t)+\nu\left(-k^2+\frac{\partial^2}{\partial y^2}\right)\hat{\omega}_k(y,t), \tag{24}$$

$$k=0,1,\ldots,N/2,$$

$$\hat{\omega}_k(y,t)+\left(-k^2+\frac{\partial^2}{\partial y^2}\right)\hat{\psi}_k(y,t)=0, \tag{25}$$

$$k=0,1,\ldots,N/2.$$

Applying now the Chebyshev-collocation method in inhomogenuous direction (*y*-axe) to the above system of equations, we get the

$$\frac{\partial \hat{\omega}_{kN}(y_j,t)}{\partial t}+\left[\widehat{\frac{\partial \psi}{\partial y}\frac{\partial \omega}{\partial x}}\right]_{kN}(y_j)-\left[\widehat{\frac{\partial \psi}{\partial x}\frac{\partial \omega}{\partial y}}\right]_{kN}(y_j)=$$

$$\hat{\mathcal{F}}_{kN}(y_j,t)+\nu\left(-k^2+\sum_{l=0}^{N}d_{j,l}^{(2)}\right)\hat{\omega}_{kN}(y_j,t), \tag{26}$$

$$k=0,1,\ldots,N/2,\quad j=1,\ldots,N-1,$$

$$\hat{\omega}_{kN}(y_j,t)+\left(-k^2+\sum_{l=0}^{N}d_{j,l}^{(2)}\right)\hat{\psi}_{kN}(y_j,t)=0, \tag{27}$$

$$k=0,1,\ldots,N/2,\quad j=1,\ldots,N-1.$$

Here $d_{j,l}^{(2)}$ are elements of second order Chebyshev differentiation matrix [2]. This sistem of eqations is discretized in time by using Adams-Bashworht semi-implicit finite difference scheme with second order accu-racy.

This system of equations (27) and (28) together with boundary conditions (16) and (17) should be solved numerically. The system is represented by 2(N+1)×2(N+1) three time levels matrix equation. The nonlinear advective terms have been computed by pseudospectral technique [3], so that full Navier-Stokes equation in vorticity-streamfunction formulation can be simulated for the case of 2D-plane channel flow. The problem of two boundary conditions for streamfunction and none for vorticity has been succesfully resolved by applying the influence matrix method [4].

$$\frac{3\hat{\omega}_{kN}^{n+1}(y_j)-4\hat{\omega}_{kN}^{n}(y_j)+\hat{\omega}_{kN}^{n-1}(y_j)}{2\Delta t}+2\left(\widehat{\frac{\partial\psi}{\partial y}\frac{\partial\omega}{\partial x}}\right)_{kN}^{n}(y_j)-$$
$$-\left(\widehat{\frac{\partial\psi}{\partial y}\frac{\partial\omega}{\partial x}}\right)_{kN}^{n-1}(y_j)+2\left(\widehat{\frac{\partial\psi}{\partial x}\frac{\partial\omega}{\partial y}}\right)_{kN}^{n}(y_j)-\left(\widehat{\frac{\partial\psi}{\partial x}\frac{\partial\omega}{\partial y}}\right)_{kN}^{n-1}(y_j) \tag{28}$$
$$+\nu k^2\hat{\omega}_{kN}^{n+1}(y_j)-\nu\sum_{l=0}^{N}d_{j,l}^{(2)}\hat{\omega}_{kN}^{n+1}(y_l)=\hat{\mathcal{F}}_{kN}^{n+1}(y_j),\ k=-N_x/2,...,N_x/2,\ y_j=\cos\pi j/N_y.$$

The initial condition for our simulation is the solution of the problem for laminar plane Couette-Poiseuille 2D-flow is given by the equation (1) where we have chose A=0.5 and B=1.Our goal is to simulate the velocity evolution for the value of Reynolds number *Re*=1000 which is beneath the critical value Re_c=5772, to simulate the transient growth of kinetic energy.

We have carried out this simulation by imposing the perturbations obtained by solution (8) , (12) and (13) to the laminar velocity profile given by (1). The simulations are driven by forcing term which is determined by perturbed Navier-Stokes equation,

$$F_{pert}=\frac{\partial}{\partial t}(\Omega+\omega')+\frac{\partial}{\partial y}(\Psi+\psi')\frac{\partial}{\partial x}(\Omega+\omega')-$$
$$\frac{\partial}{\partial x}(\Psi+\psi')\frac{\partial}{\partial y}(\Omega+\omega')-\nu\left[\frac{\partial^2}{\partial x^2}(\Omega+\omega')+\frac{\partial^2}{\partial y^2}(\Omega+\omega')\right]. \tag{29}$$

Here Ω and Ψ are the values determined from (1)and (4).

$$\vec{V}=rot\vec{\Psi},\quad \vec{\Omega}=rot\vec{V} \tag{30}$$

The results of simulation of nonlinear perturbation evolution are presented in the figures 1, 2 and 3.

4. Optimization of initial perturbation

We have carried out this simulation by imposing the perturbations obtained by solution of Orr-Sommerfeld equation on laminar velocity profile, in the case of stream function it reads

$$\psi'(x,y,t)=\sum_{n=1}^{N'}\beta_n\hat{\psi}_n(y)e^{i\alpha(x-c_nt)}=$$
$$=\sum_{n=1}^{N'}\beta_n\hat{\psi}_n(y)e^{i\alpha\left(x-(c_{Re}+ic_{Im})_nt\right)}, \tag{31}$$

where $\hat{\psi}_n$'s are eigenvectors and c_n's are eigenvalues of generalized eigenvalue problem of Orr-Sommerfeld equation for the case of plane Poiseuille flow, and β_n are coeffiecient which should be determined by appropriate optimization procedure. Here $\boldsymbol{\beta}$ is perturbation

spectrum obtained by using the matrix Ψ, whose columns are eigenvectors $\hat{\psi}_n(y)$, in the following way.

$$\boldsymbol{\beta} = \Psi^{-1}\boldsymbol{\psi}'(y,0). \tag{26}$$

Functional to be minimized is

$$f = \boldsymbol{\psi}'^{*} \bullet \boldsymbol{\psi}' = (\Psi\boldsymbol{\beta})^{*} \bullet (\Psi\boldsymbol{\beta}) = \boldsymbol{\beta}^{*} \bullet \Psi^{*}\, \Psi\boldsymbol{\beta} = \boldsymbol{\beta}^{*} \bullet A\boldsymbol{\beta}. \tag{27}$$

In other words,the fuctional is the dot product of perturbation vector of stream function and its complex conjugate. If we put the condition that the *i-th* mode is of unit magnitude, then the variational problem can be reduced to the following function

$$f = \boldsymbol{\beta}^{*} \bullet A\boldsymbol{\beta} + \lambda(\boldsymbol{\beta} \bullet \boldsymbol{e}_i - 1), \tag{28}$$

where we have designated with e_i – the unit vector, i.e. the column vector whose the only element different from null is the *i-th* element. Let find the derivative with respect to $\boldsymbol{\beta}$, e.i. let find the first variation of the above function *f* and equal it with zero, so that we have

$$\frac{d\,f}{d\boldsymbol{\beta}} = \frac{d}{d\boldsymbol{\beta}}\left[\boldsymbol{\beta}^{*} \bullet A\boldsymbol{\beta} + \lambda(\boldsymbol{\beta} \bullet \boldsymbol{e}_i - 1)\right] = A\boldsymbol{\beta} + \lambda\,\boldsymbol{e}_i = \mathbf{0}. \tag{29}$$

And after rearrengments

$$A\boldsymbol{\beta} = -\lambda\,\boldsymbol{e}_i, \tag{30}$$

so that after multiplication both side with inverse matrice A^{-1} from the left, we have

$$\boldsymbol{\beta} = -\lambda\, A^{-1}\boldsymbol{e}_i. \tag{31}$$

The optimizated spectrum can be normalized by appropriate calculation of coefficient λ, so that the value $\beta_i = 1$ can be obtained. The value of λ has been determined by this expression

$$\lambda = \frac{-\beta_i}{a_{ii}^{-1}} = \frac{-1}{a_{ii}^{-1}}. \tag{32}$$

In the fig.1 and fig.2 are shown the vorticity fields for ten different times, for dimensionless time $t = n\pi$, $n = 1,...,10$. The perturbation is optimized to the least stable eigenvalue $c = 0.9362 - i\ 0.06138$ and for $Re = 1000$. This optimization of perturbation is capable of expressing the initial transient energy growth [8] [9],[10] [11].

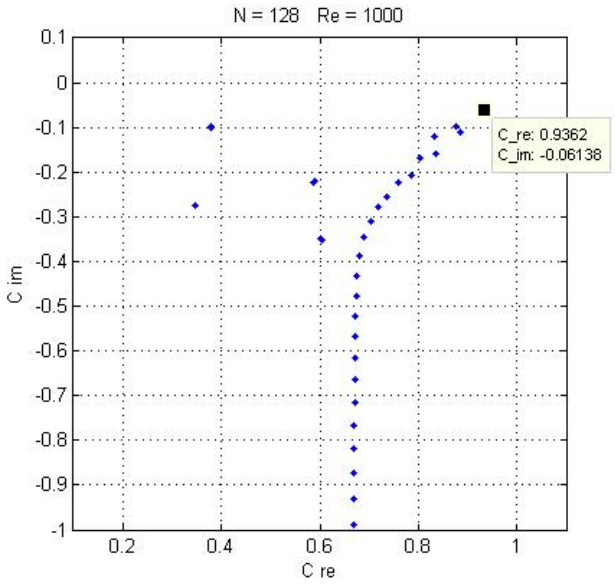

Figure 1. Eigenvalues obtained as Orr-Sommerfeld spectrum of plane Coette-Poiseuille flow for Re=1000 and wave number $\alpha = 1.5$ and $\beta = 0$. The least stable value for S branch is $c = 0.0.9362 - i\ 0.06138$

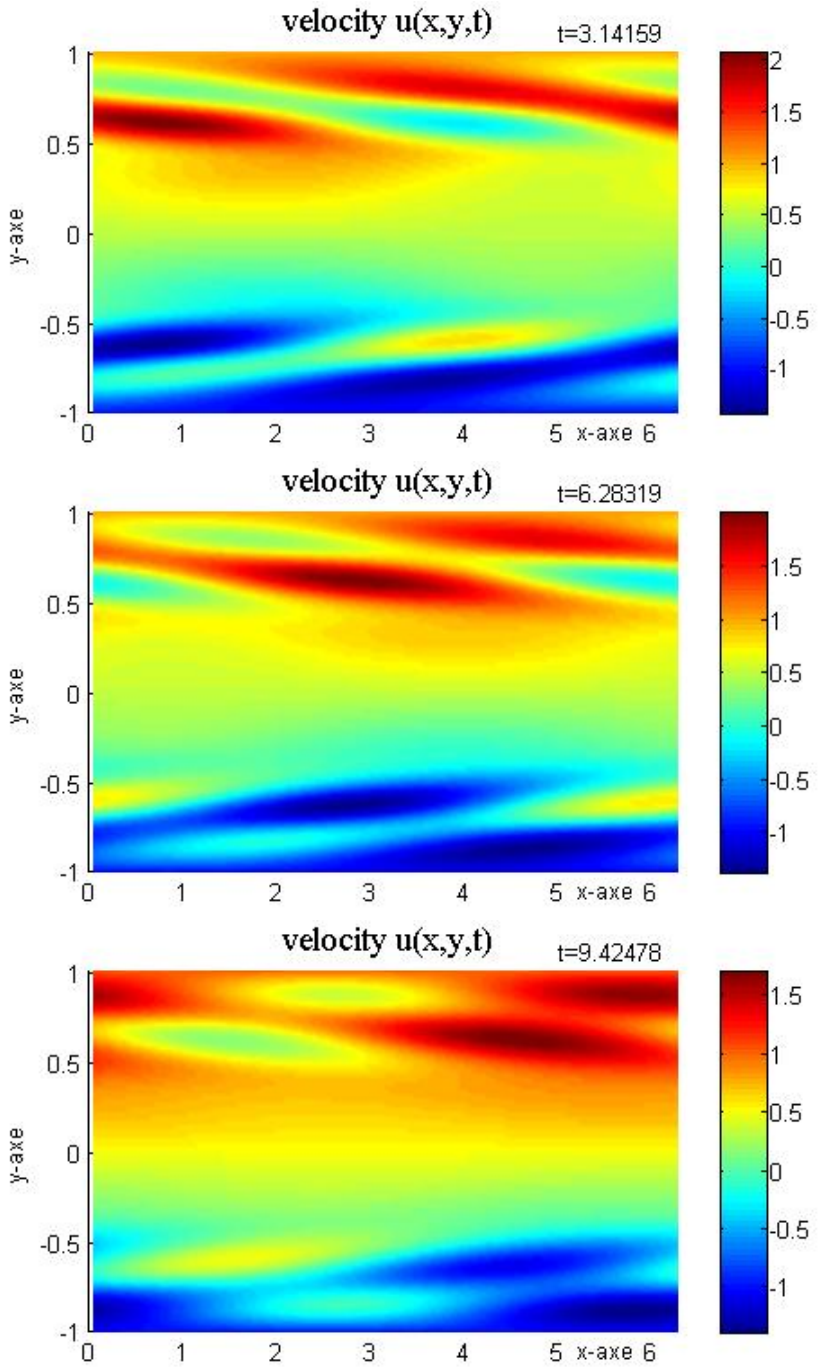

Figure 2. Velocity evolution in perturbed Poiseuille-Couette flow

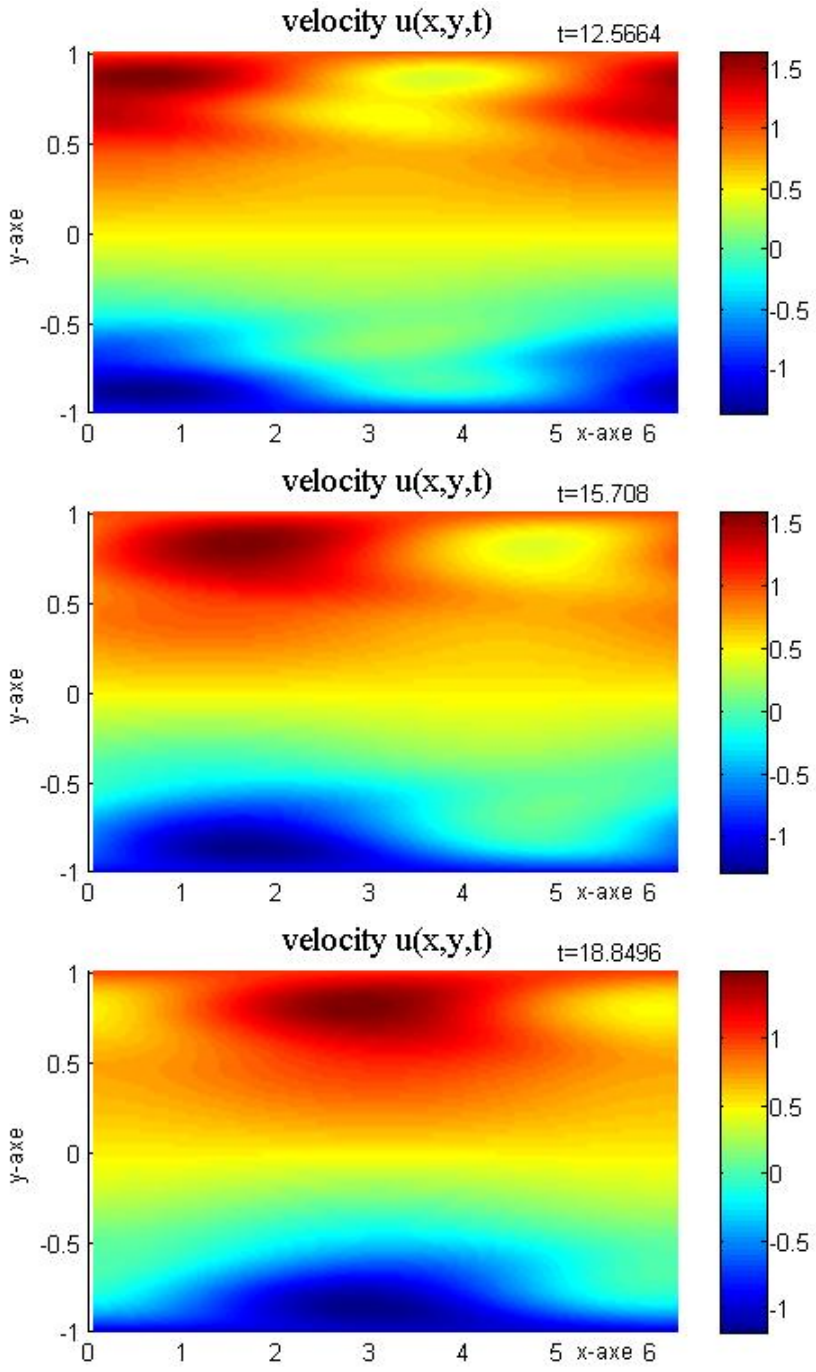

Figure 3. Velocity evolution in perturbed Poiseuille-Couette flow

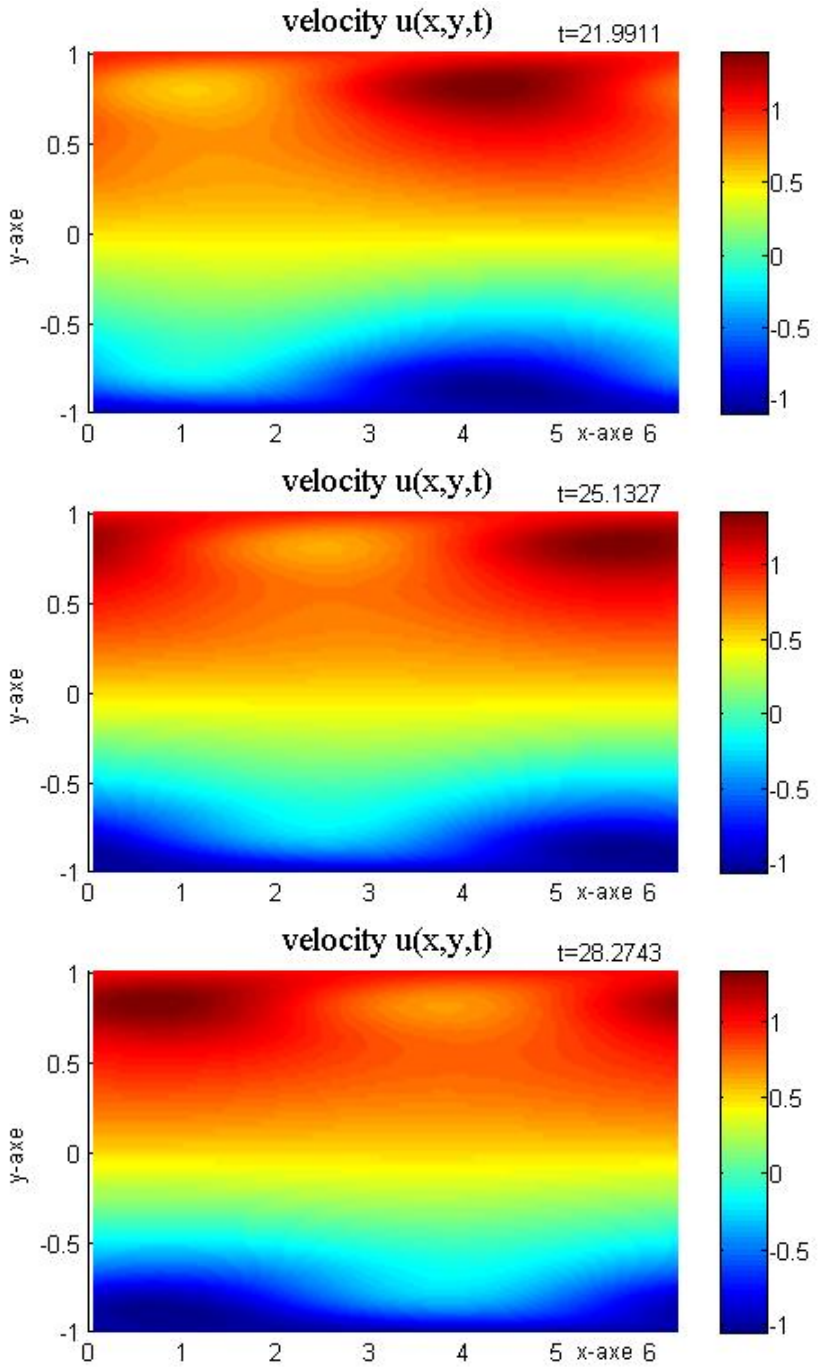

Figure 4. Velocity evolution in perturbed Poiseuille-Couette flow

5. Results of simulation

In the nonlinear evolution of perturbations shown in the figures 2 , 3 and 4 we can notice that the kinetic energy of perturbations has initial optimized perturbation which steadily decreases in the time interval $0<t<5\pi$. It can be seen from colorbars at the right-hand side, where maximal values of velocity goes to $u_{max}(x=1,y=0.6)=2.07$ at $t=\pi$ and $u_{max}(x=3,y=0.6)=1.8$ at $t=2\pi$. It can also be noticed that the maximal posistive and negative velocity perturbations are concentrated in the region of y=0.6 and y=-0.6. for $t=2\pi$. In the instant of time $t=3\pi$ we can see that in the middle of the channel (y=0) where the velocity for Couette flow should be zero and for our plane Couette-Poiseuille flow is u=0.5 for unperturbed flow, for this perturbed flow we have that velocity is almost uperturbed, and that the perturbations are restricted only to the critical layer where the velocity of fluid and velocity of perturbed wave have the same speed.
After the kinetics energy has attained its maximum in the initial stage and decreases steadily afterwards, we can see on right-hand side on colorbars that the maximal velocities have less values that it has in the privious instatn of time. We have almost the whole time interval $0<t<9\pi$ where the kinetic energy of perturbations dies out, and decreases steadily. The middle of the channel remain from the instant of time $t=3\pi$ practicaly uperturbed along the x-direction, since we see the straight yellow line all the time. In this period of time two mayor perturbations are simetrical with respect to y=0 and travel at the same speed. For the instant of time $t=9\pi$ we can see that the veloctity profile is almost uperturbed and is very close to the laminar flow described by the exact analytical solution of Navier Stokes equation given by expression (1) for A=1/2 and B=1.

6. Conclusions

We can see that for Re=1000 which is beneath the critical values for Poiseuille flow (Re_c=5722), and having in mind that the Couette flow is stable for all values of Reynolds numbers, we have shown the results of simulation which does not exhibit in some interval of time significant growth of fluid flow kinetic energy, so that the flow is stable in this time interval. Since we have simulated 2D Navier Stokes equation, very significat term which describes vortex streching is absent (it exist in 3D Navier-Stokes equations). If this term were included in the simulation, we believe that this achieved transienth growth would be sufficient to trigger further develoment to full turbulent flow. So we have shown for this case that the limit time interval can exist where perturbations grow but 2D Navier-Stokes equations are not capable of transfering energy from big to small scales, but only the inverse cascade, only from small to big scales

References

[1] JOVANOVIĆ M. (2009); *Simulation of temporal hydrodynamic stability in plane channel viscous flow*; 2nd international congress of Serbian Society of Mechanics, (IConSSM), Palić , Subotica , Serbia, 1-5 June 2009. p. B 03.
[2] JOVANOVIĆ M. , NIKODIJEVIĆ J. (2010), *Vorti-city simulation in a plane channel flow*, X Trienial Intenational SAUM Conference on System, Automatic control and measurements, Niš, Serbia 10th-12th November 2010, Proceedings pp.327-330.
[3] FORNBERG B. (2005), *Pseudospectral methods*, Cambridge University Press.
[4] KLEISER L., SCHUMANN U. (1980) *Treatment of incompressibility and boundary conditions in 3D numerical spectral simulation of plane channel flows*Hirschel E.H.(ed.): Third GAMM Conference Numerical Methods in Fluid Dynamics, Vieweg, Braunschweig, pp.165-173.
[5] ORSZAG S.A., (1971), *Accurate solution of the Orr-Sommerfeld stability equation*, Journal of Fluid Mechanics, vol.50, pp. 689-703.
[6] SCHMID P., HENNINGSON D. (2002), *Stability and Transition in Shear Flows* , Springer.
[7] CRIMINALE W.O., JACKSON T.L., JOSLIN R.D., (2003), *Theory and Computation in Hydrodynamic Stability*, Cambridge University Press.
[8] TREFETHEN L.N., TREFETHEN A.E., REDDY S.C., DRISCOLL T.A., (1993), *Hydrodynamic stability without eigenvalues*, Science, vol.261, p.578.
[9] REDDY S.C., HENNINGSON D.S.,(1993), "*Energy growth in viscous channel flows*" , J.Fluid Mech., vol 252, p.209.